The Ny-Ålesund Aerosol Cloud Experiment (NASCENT): Overview and First Results

J. T. Pasquier* (1) and R. O. David (2) and G. Freitas (3,4) and R. Gierens (5) and Y. Gramlich (3,4) and S. Haslett (3,4) and G. Li (1) and B. Schäfer (2) and K. Siegel (3,4) and J. Wieder (1) and K. Adachi (17) and F. Belosi (14) and T. Carlsen (2) and S. Decesari (14) and K. Ebell (5) and S. Gilardoni (12,13) and M. Gysel-Beer (9) and J. Henneberger (1) and J. Inoue (6) and Z. A. Kanji (1) and M. Koike (7) and Y. Kondo (6) and R. Krejci (3,4) and U. Lohmann (1) and M. Maturilli (10) and M. Mazzolla (12,13) and R. Modini (9) and C. Mohr (3) and G. Motos (11) and A. Nenes (11, 19) and A. Nicosia (14) and S. Ohata (15, 16) and M. Paglione (14) and S. Park (8) and R. E. Pileci (9,21) and F. Ramelli (1) and M. Rinaldi (14) and C. Ritter (10) and K. Sato (18) and T. Storelvmo (2) and Y. Tobo (6) and R. Traversi (20) and A. Viola (12,13) and P. Zieger†(3,4)

(1) Institute for Atmospheric and Climate Science, ETH Zürich, Zurich, Switzerland

(2) Department of Geosciences, University of Oslo, Oslo, Norway

(3) Department of Environmental Science, Stockholm University, Sweden

(4) Bolin Centre for Climate Research, Stockholm University, Sweden

(5) Institute for Geophysics and Meteorology, University of Cologne, Cologne, Germany

(6) National Institute of Polar Research (NIPR), Tachikawa, Tokyo, Japan

(7) Department of Earth and Planetary Science, Graduate School of Science, University of Tokyo, Tokyo, Japan

(8) Korea Polar Research Institute (KOPRI), Incheon, Korea

Early Online Release: This preliminary version has been accepted for publication in *Bulletin of the American Meteorological Society*, may be fully cited, and has been assigned DOI 10.1175/BAMS-D-21-0034.1. The final typeset copyedited article will replace the EOR at the above DOI when it is published.

(9) Laboratory of Atmospheric Chemistry, Paul Scherrer Institute (PSI), Villigen PSI, Switzerland

(10) Alfred Wegener Institute, Helmholtz Centre for Polar and Marine Research (AWI), Potsdam, Germany

(11) Laboratory of Atmospheric Processes and their Impacts, Ecole Polytechnique Fédérale de Lausanne, Lausanne, Switzerland

(12) Institute for Polar Sciences, CNR, Bologna, Italy

(13) Institute for Polar Sciences , CNR, Rome, Italy

(14) National Research Council, Institute of Atmospheric Sciences and Climate, CNR-ISAC, Bologna, Italy

(15) Institute for Space–Earth Environmental Research, Nagoya University, Nagoya, Aichi, Japan

(16) Institute for Advanced Research, Nagoya University, Nagoya, Aichi, Japan

(17) Meteorological Research Institute, Tsukuba, Ibaraki, Japan

(18) Kitami Institute of Technology, Kitami, Hokkaido, Japan

(19) Center for Studies of Air Quality and Climate Change, Institute for Chemical Engineering Sciences, Foundation for Research and Technology Hellas, Patras, Greece

(20) Department of Chemistry, University of Florence, Florence, Italy

(21) U-Earth Biotech Ltd, London, United Kingdom

[*] *Corresponding author*: Julie T. Pasquier, julie.pasquier@env.ethz.ch

[†] *Corresponding author*: Paul Zieger, paul.zieger@aces.su.se

Accepted for publication in *Bulletin of the American Meteorological Society*. DOI 10.1175/BAMS-D-21-0034.1.

ABSTRACT

The Arctic is warming at more than twice the rate of the global average. This warming is influenced by clouds which modulate the solar and terrestrial radiative fluxes, and thus, determine the surface energy budget. However, the interactions among clouds, aerosols, and radiative fluxes in the Arctic are still poorly understood. To address these uncertainties, the Ny-Ålesund AeroSol Cloud ExperimeNT (NASCENT) study was conducted from September 2019 to August 2020 in Ny-Ålesund, Svalbard. The campaign's primary goal was to elucidate the life cycle of aerosols in the Arctic and to determine how they modulate cloud properties throughout the year. In-situ and remote sensing observations were taken on the ground at sea-level and at a mountaintop station, and with a tethered balloon system. An overview of the meteorological and the main aerosol seasonality encountered during the NASCENT year is introduced, followed by a presentation of first scientific highlights. In particular, we present new findings on aerosol physicochemical properties which also include molecular properties. Further, the role of cloud droplet activation and ice crystal nucleation in the formation and persistence of mixed-phase clouds, and the occurrence of secondary ice processes, are discussed and compared to the representation of cloud processes within the regional Weather Research and Forecasting model. The paper concludes with research questions that are to be addressed in upcoming NASCENT publications.

Capsule summary. The NASCENT campaign was dedicated to study, in unprecedented detail by using various novel methods, how aerosols, clouds and their interactions influence the Arctic climate over the course of one year at Ny-Ålesund, Svalbard.

1. Motivation

Average temperatures over the Arctic region have increased by a factor of 2 to 3 compared to the global average rate in the past few decades (e.g., Wendisch et al. 2017). This phenomenon is known as Arctic Amplification (AA) and causes the retreat of sea ice at the alarming rates currently observed (e.g., Bennartz et al. 2013; Cohen et al. 2014). Several feedback mechanisms contribute to AA, but their relative importance in different regions of the Arctic is still under discussion (e.g., Hall et al. 2021). The sea-ice albedo feedback is often proposed as the main driver of AA (e.g., Deser et al. 2000). However, model experiments have shown that AA occurs even in the absence of sea ice and snow cover changes (e.g., Graversen and Wang 2009). Despite their potentially large impact on the AA, the feedback processes related to aerosols and clouds are especially poorly understood (e.g., Morrison et al. 2011; Pithan and Mauritsen 2014; Wendisch et al. 2017; Goosse et al. 2018).

The role of aerosols in the Arctic climate is especially complex due to the diverse processes that control their abundance and their chemical and physical properties (e.g., Willis et al. 2018). Knowledge gaps in aerosol sources, sinks, transformation processes and uncertainties in aerosol-cloud interactions are among the reasons why current climate models have difficulties reproducing the current and future climate in the Arctic (Schmale et al. 2021). At Ny-Ålesund on Svalbard, the potential aerosol particle sources and sinks show a strong seasonality (Tunved et al. 2013; Ström et al. 2003). Primary particles can originate from natural sources such as oceans (e.g., sea spray, primary biological particles) or glaciers (e.g., soil dust) (Weinbruch et al. 2012; Tobo et al. 2019; Heslin-Rees et al. 2020). Particles from forest fires or anthropogenic emissions can be transported from lower latitudes to Svalbard (Stohl et al. 2007; Schacht et al. 2019). Secondary particles can be formed locally from gas-to-particle conversion processes involving anthropogenic and natural precursor gases (e.g., Dall'Osto et al. 2017; Nielsen et al. 2019; Beck et al. 2020; Lee et al. 2020a; Brean et al. 2021; Choi et al. 2019). However, quantitative knowledge about the physicochemical properties of Arctic aerosols and precursor gases remains limited, especially during the Arctic winter, which renders an accurate source apportionment and the estimation of their impact difficult.

Clouds influence down-welling solar and terrestrial radiative fluxes that determine the surface energy budget (e.g., Curry et al. 1996; Shupe and Intrieri 2004). On the one hand, clouds scatter solar radiation back to space, leading to a shortwave cooling effect at the surface. On the other hand, they emit longwave radiation to space and back to the surface, and therefore have a longwave warming effect at the surface (Lohmann et al. 2016; Nomokonova et al. 2019; Ebell et al. 2020). The impact clouds have on the energy budget depends on their macro- and microphysical properties (e.g., Shupe and Intrieri 2004; Dong et al. 2010; Sedlar et al. 2012). The optical thickness of a pure ice cloud is lower for a given cloud water path because ice particles are fewer and larger than corresponding liquid droplets and have a different refractive index, i.e. ice clouds have lower albedos and longwave emmisivities (Sun and Shine 1994; Korolev 2007). Arctic mixed-phase clouds (MPCs), consisting of cloud droplets and ice crystals, particularly influences the Arctic surface radiation balance (e.g., Curry et al. 1996; Shupe and Intrieri 2004; Goosse et al. 2018). Their albedos and emissivities lie between the ones of pure ice and pure liquid clouds, and depend on the exact mixture of the phases (Sun and Shine 1994) which is strongly influenced by aerosols. Aerosols acting as cloud condensation nuclei (CCN) are required to form cloud droplets and aerosols termed ice-nucleating particles (INPs) are needed to form primary ice crystals. Once primary ice crystals are formed, secondary ice production (SIP) can occur (e.g., Hallett and Mossop 1974; Takahashi et al. 1995; Korolev et al. 2020; Korolev and Leisner 2020) and enhance the ice crystal number concentration (ICNC) by several order of magnitudes (Korolev et al. 2020). Consequently, aerosol particles acting as CCN and INPs as well as SIP determine the phase partitioning within MPCs, which ultimately influences the radiation budget.

The phase partitioning within MPC impacts the lifetime of Arctic MPCs. The mixture of ice crystals and cloud droplets is thermodynamically unstable and the so-called Wegener-Bergeron-Findeisen (WBF) process (Wegener 1911; Bergeron 1935; Findeisen 1938) can cause a complete glaciation of the cloud within a few hours (Harrington et al. 1999; Rangno and Hobbs 2001; Korolev and Isaac 2003). However, Arctic MPCs are surprisingly persistent over several hours or days (e.g., Zuidema et al. 2005; Morrison et al. 2011). The current understanding obtained from modelling and theoretical studies is that self-maintaining feedbacks between liquid water, radiation, and turbulent updrafts are responsible for the persistence of Arctic MPCs (Morrison et al. 2011). Although a number of studies have focused on the microphysical properties of Arctic MPCs (e.g., McFarquhar et al. 2011; Lloyd et al. 2015; Young et al. 2016; Wendisch et al. 2019), the processes controlling the life cycle of Arctic MPCs still remain poorly understood (e.g., Tjernström et al. 2014; Mioche et al. 2015).

The Ny-Ålesund AeroSol Cloud ExperimeNT (NASCENT) campaign was conducted to enhance our knowledge on Arctic aerosols and clouds, and their complex interactions throughout the polar year. The former mining town of Ny-Ålesund, located on the western part of the Norwegian archipelago of Svalbard (Fig. 1), is nowadays fully dedicated to research. Ny-Ålesund is a unique place to study aerosols-cloud interactions and their potential influence on climate as the Svalbard region is frequently covered by MPCs susceptible to aerosol perturbations (Mioche et al. 2015) and experiences the largest warming within the Arctic (Dahlke and Maturilli 2017; Susskind et al.

2019). The NASCENT study was designed to obtain a comprehensive set of cloud and aerosol observations to address in particular the following questions:

- What are the factors that determine the ability of aerosol particles to act as CCN and INPs in the Arctic?
- What are the sources, precursor gases, chemical composition, molecular properties, and the seasonality of these cloud forming aerosols?
- Under which conditions do INPs or SIP dominantly influence the phase partitioning in Arctic MPCs?

The general setup and main instrumentation of NASCENT are introduced in Section 2. An overview of the temperature, wind, aerosol, and cloud seasonality during NASCENT is given in Section 3. In Section 4, first research highlights on aerosol and cloud interactions are discussed. Finally, a summary is given in Section 5, including questions to be answered in the forthcoming data analyses of the NASCENT study.

2. NASCENT study design

a. Measurement site

The NASCENT study took place at Ny-Ålesund (78.9° N, 11.9 ° E), located on the west coast of Svalbard, from September 2019 through August 2020. Ny-Ålesund is situated on the south side of Kongsfjorden and surrounded by glaciers, moraines, rivers, mountains, and a typical tundra ecosystem. During NASCENT, atmospheric measurements were performed at five locations close to Ny-Ålesund (Fig. 1). The atmospheric observatory of the AWIPEV research base and the Swiss Site are located at the southwestern edge of town. The Zeppelin Observatory is located 2 km southwest of Ny-Ålesund at 475 m a.s.l. Further measurements were performed at the Gruvebadet laboratory located about 1 km southwestward and at the Amundsen-Nobile Climate Change Tower (CCT) 1 km southwestward of the town.

b. Experimental set-up

Aerosol, cloud, radiation and meteorological properties were characterized using a multifaceted suite of instrumentation ranging from in-situ to remote sensing techniques. An overview of the retrieved parameters at the different locations is given in Figure 1 and in Table 2. Further details of the set-up and a table with the data coverage are provided in the supplementary information (SI). At the Zeppelin Observatory (see e.g., Platt et al. 2021, for a review of the last 30 years of observations), detailed aerosol and cloud in-situ observations and meteorological parameters were taken using a multitude of complementary instrument techniques. At the temporary Swiss Site, ambient aerosol, CCN, and INP concentrations (INPC) were sampled through an heated inlet mounted on top of the measurement container. The holographic imager HOLIMO3B was mounted on the tethered balloon system HoloBalloon (Ramelli et al. 2020) to obtain in-situ phase-resolved particle size distributions up to an altitude of 1000 m a.s.l. At the AWIPEV Observatory, long-term measurements are conducted to monitor the Arctic atmosphere including a cloud radar, a ceilometer, and a wind lidar. During intensive observation periods, additional radiosondes were launched to supplement the standard daily launches. Furthermore, meteorological parameters (e.g. temperature, humidity, wind speed and direction) and surface-based radiation fluxes were monitored (Maturilli et al. 2013; Maturilli 2020). At Gruvebadet, aerosol properties (e.g., Becagli et al. 2019; Turetta et al. 2021), black carbon (BC) concentration, INPC, and chemical characterization of organic aerosol (PM1) were monitored. Furthermore, wind speed and direction, temperature, and radiation were measured on the 33 m high CCT. Note that because of the distance between the five measurement locations, there are small spatial (up to 2 km) and temporal (up to a few minutes) differences between the measurements at the different sites. The combination of these measurements provides the opportunity to investigate aerosol-cloud interactions in the Arctic at an unprecedented scale. To exemplify the use of this multifaceted data set, we use the Advanced Weather Research and Forecasting (WRF) model, version 4.2.1 (Skamarock et al. 2019), to evaluate the model representation of a MPC when prescribing the measured CCN and INP concentrations.

3. Seasonality of meteorological, aerosol, and cloud parameters during NASCENT

a. Temperature

During NASCENT, unusually cold temperatures during the winter and spring (up to 6°C colder) were experienced (Fig. 2a). The anomalously cold temperatures during February and March can be attributed to the exceptionally strong and cold stratospheric polar vortex (Lawrence et al. 2020; Lee et al. 2020b). The low temperatures caused the rare freezing of the Kongsfjorden from February to April 2020, which likely limited the emission of local biological aerosols from the fjord. Although this may have led to a lower abundance of aerosol particles, no significant deviation from previous observations was observed (Fig. 3a). During the summer months, above normal temperatures were observed (up to 2°C, Fig. 2a) but with little to no detectable changes in the cloud and aerosol climatologies (Figs. 2b and 3).

b. Wind

The wind at Ny-Ålesund is strongly influenced by the surrounding topography, especially by the mountains, Kongsfjorden, and the glaciers. The wind measured 10 m above ground on the measurement field of the AWIPEV Observatory predominantly came from the southeast and less frequently from the southwest and northwest (Fig. 4). The wind speed was generally moderate (below 9 m s^{-1}). These results are in agreement with previous studies showing that the wind is channeled along the Kongsfjorden (Beine et al. 2001; Maturilli et al. 2013; Maturilli and Kayser 2017). The effect of topography can be seen when comparing the wind measurements at AWIPEV to the ones taken at the CCT where the main wind direction was also from the southeast but had more frequent periods of southwesterly wind (Fig. 4), which is related to the katabatic outflow from the Brøggerbreen glaciers channeled along the slopes of the Zeppelin mountain range (Maturilli et al. 2013). As the surface air flow is determined by the topography, local aerosol sources are likely to dominate over large-scale transport of aerosol under stable atmospheric conditions at these locations around Ny-Ålesund.

At the Zeppelin Observatory, the prevailing wind showed more southerly components with occasional periods of north- to northwesterly wind (Fig. 4), which is in agreement with previous studies (Beine et al. 2001). This dominant wind component is due to the channeling between Zeppelin mountain on the southwest side and a smaller hill on the east side of the observatory. This mountain blocks the large-scale winds and are responsible for the relatively low wind speed at the observatory (mostly below 6 m s^{-1}). Nevertheless, the air at Zeppelin Observatory is often above the local inversion and therefore, less influenced by local aerosol sources compared to the other sites around Ny-Ålesund (e.g., Platt et al. 2021) as shown below.

Consistent with the surface winds being influenced by the terrain surrounding Ny-Ålesund, the radiosonde measurements between 3000 m and 3500 m a.s.l. show that southwesterly to northwesterly winds were most frequently observed above Ny-Ålesund (Fig. 4), in agreement with the climatological wind observed by Maturilli and Kayser (2017).

c. Aerosols

Aerosol particles at Ny-Ålesund follow a typical seasonal cycle that is governed by the seasonality of the particles' respective sources and sinks (e.g., Tunved et al. 2013; Freud et al. 2017), and the seasonality in atmospheric transport patterns (e.g., Stohl 2006). The summer months are marked by high number concentrations of small particles (i.e., with a diameter ≤ 100 nm) due to frequent new particle formation events (e.g., Tunved et al. 2013; Dall'Osto et al. 2017; Beck et al. 2020). In contrast, aerosol mass tends to reach a maximum in the winter and spring months (e.g., Ström et al. 2003) due to long-range transport of pollutants that form the well-known Arctic haze (e.g., Shaw 1995; Quinn et al. 2007). BC concentrations follow the aerosol mass cycle and peak during winter and spring (Eleftheriadis et al. 2009; Sinha et al. 2017).

The typical seasonal cycle of aerosol loading was also observed during NASCENT, as can be seen in Figure 3, which shows the monthly distributions of daily-averaged particle number and BC mass concentrations measured at the Zeppelin Observatory and at Gruvebadet in the valley. The observed aerosol number concentrations (Fig. 3a) at both sites show the same seasonal cycle with a maximum in July and a minimum in the late fall and early winter months, similar and within a factor of two of previous observations (Tunved et al. 2013). This difference, primarily during summer months, can be attributed to different measurement methods: Tunved et al. (2013) used integrated particle number concentrations (using size-resolved measurements), while we used the direct particle concentration measurements using condensation particle counters (CPC) that have a lower particle cut-off diameter and are less influenced by particle diffusion losses.

The BC concentrations were slightly higher in Gruvebadet than at the Zeppelin Observatory, especially throughout 2020, which is most likely due to local emissions from the Ny-Ålesund settlement that impact the Gruvebadet site but not necessarily the mountain-top site, especially during shallow boundary layers (Dekhtyareva et al. 2018; Platt et al. 2021).

As shown in Figure 3b, the BC levels measured during NASCENT were comparable to values reported previously at the Zeppelin Observatory (Eleftheriadis et al. 2009). For example, during the pristine summer and autumn, monthly-mean BC concentrations at the Zeppelin Observatory amounted only to a few ng m^{-3}, which are comparable to values measured over the remote southeast Pacific (Shank et al. 2012) and the Southern Ocean (Schmale et al. 2019).

d. Clouds

During NASCENT, the monthly cloud cover assessed using the Cloudnet target classification product (Illingworth et al. 2007) ranged between 50% and 85%, out of which 30-70% had cloud tops below 3 km (Fig. 2b). The low-level cloud occurrence peaked in March 2020 and was at a minimum in December 2019 and January 2020. Liquid-only clouds were primarily observed in the summer and early autumn months. Meanwhile, MPCs and ice clouds were present year round with ice clouds being the most abundant cloud type except for below 3 km where MPCs were dominant (Fig. 2b). These observations are in accordance with measurements of liquid droplets year-round at the Zeppelin Observatory (Koike et al. 2019). Previous studies investigating cloud cover in Ny-Ålesund have observed similar cloud occurrences albeit with slight differences in seasonality and cloud type contributions (Nomokonova et al. 2019; Gierens et al. 2020). Regardless of this year to year variability, MPCs are overall the most prevalent cloud type close to the surface at Ny-Ålesund. This highlights the importance of low-level MPCs year-round in the Arctic region and their potential to alter the Arctic climate.

4. First research highlights from the NASCENT study

First highlights are described in the following sections to demonstrate how the wide variety of observations contributes to the understanding of properties and interactions of Arctic aerosols and clouds and their subsequent representation in models. We use measurements mainly taken on 12 November 2019 to discuss the role of physical and chemical aerosol properties, cloud droplet activation, ice crystal nucleation, and SIP on the formation and evolution of a MPC, and finish

Accepted for publication in *Bulletin of the American Meteorological Society*. DOI 10.1175/BAMS-D-21-0034.1.

with a comparison of the cloud structure representation in the WRF model with the in-situ cloud observations.

On 12 November 2019, a warm front influenced the weather around Ny-Ålesund (see section S1 and Fig. S1 in the SI). The temperature varied between -3 °and 0 °C at Ny-Ålesund and between -5 °and -3.5 °C at the Zeppelin Observatory. A persistent MPC was observed until 2100 UTC, with cloud top rising from 1300 to 2000 m a.s.l and cloud top temperature varying between -13.5 °C and -11 °C (Fig. S3). The cloud base varied between 200 m a.s.l. and 600 m a.s.l. (not show). The large-scale wind measured by the radiosondes (Fig. S7) and visible on the wind lidar measurements above 800 m a.s.l. (Fig. S2) was southwesterly.

a. Chemical and physical properties of aerosols and cloud residuals

At the Zeppelin Observatory, the cloud particle number concentration (CPNC) and liquid water content (LWC) reached up to $17.5\,\mathrm{cm}^{-3}$ and $0.3\,\mathrm{gm}^{-3}$, respectively (Fig. 5a). To assess the size and chemistry of the particles involved in cloud formation, the Counterflow Virtual Impactor (CVI) inlet was used to separate cloud particles from interstitial aerosol. The CVI was in operation for most of the time (Fig. 5b) and the cloud residual number concentration was very low and, as expected, inversely proportional to the visibility (on average ~560 m), which acts as a measure for the optical density of the cloud. The cloud residual size distribution was dominated by small particles of around 10 to 30 nm (Fig. 5c). These small particles were also present, although to a slightly lower extent, in the whole-air inlet, which samples both interstitial and cloud particles. It is also interesting that the accumulation mode particles (particles between 50 and 200 nm), as measured by the whole-air inlet, were found to a much lower extent within the cloud residuals and thus were probably not CCN and/or INPs at Zeppelin. A possible explanation for this is that the WBF process had occurred and liquid droplets (activated accumulation mode particles) evaporated in the presence of ice, which has been previously observed in MPCs at other mountain sites (Verheggen et al. 2007).

The origin of the enhanced number of small cloud residuals is not fully clear and a number of possibilities (e.g., SIP) and sampling artefacts are discussed in Karlsson et al. (2021). While previous studies (Karlsson et al. 2021) were missing detailed information on the cloud phase, the holographic imager HOLIMO3G (Beck et al. 2018) allows the determination of ICNC (between 25 µm and 2 mm), and the fog monitor the determination of CPNC (between 3 µm and 50 µm) in parallel to the CVI sampling. Even if the exact magnitude of the CVI sampling efficiency still remains to be solved, a good temporal agreement of the ICNC and CPNC with the cloud residual number concentration (Fig. 5d) indicates that sampling artefacts is an unlikely explanation for the small sizes of cloud residual and suggests that indeed, SIP and the WBF process may cause such small cloud residuals. The cloud residual measurements observed during NASCENT, in combination with the high-resolution cloud probes, will provide new and unique evidence of the importance of sub-accumulation mode particles on cloud formation in the Arctic.

The chemical composition of aerosols, aerosol precursor gases, and cloud residuals at the molecular level was investigated using the FIGAERO-CIMS. On the 12th of November 2019, the instrument only sampled the gas phase. Therefore, to illustrate the capability of this analytical tool for the aerosol particle phase, here we present an example from 24 December 2019. On this day, a low-level MPC (cloud top below 2 km) was observed and the ground temperatures were varying between -9° and -6°C at Ny-Ålesund. Figures 6a,b, show a comparison of the chemical composition of aerosol particles before a cloud event to aerosol particles that were activated as INPs or CCN (cloud residuals). The ~400 organic compounds identified in the particle phase by FIGAERO-CIMS are grouped based on their number of carbon and oxygen atoms, and the signal of groups with the same carbon numbers are stacked. To our knowledge this is the first time that such a detailed chemical analysis is shown for Arctic cloud residuals.

Molecules with up to 20 carbon atoms and 10 oxygen atoms were identified in both the pre-cloud aerosol and cloud residuals. The majority of the pre-cloud aerosol mass was from compounds with up to 10 carbon atoms. A prominent contribution from $C_6H_{10}O_5$, likely levoglucosan, a marker for biomass burning emissions, was observed. This indicates long-range transport of pollution from wintertime solid fuel combustion on the Eurasian continent as a potential source for particle components observed here. However, the biomass burning chemical signature was not observed in the cloud residuals. The cloud residual chemical composition showed relatively smaller contributions of compounds with up to 10 carbon atoms and more than 5 oxygen atoms (see Fig. 6), and relatively higher contribution of compounds with larger carbon chains and 2 oxygen atoms, potentially fatty acids. These first results could indicate that the organic fraction relevant for cloud formation in the Arctic consists of molecules with rather long carbon chains, at least in the winter months.

Simultaneous measurements of organic aerosol chemical composition via H-NMR from ambient PM1 filter samples at Gruvebadet on 24 December 2019 are qualitatively comparable to those of the FIGAERO-CIMS at the Zeppelin Observatory. In particular, as highlighted in Figure 6c, the H-NMR confirms the presence of levoglucosan and aromatic compounds (e.g., phenols and methoxy-phenols), further supporting the possible long-range transport of biomass burning emissions from the continents. This feature is common during the winter season (Zangrando et al. 2013; Feltracco et al. 2020). These samples are also impacted by high contributions of hydroxymethane-sulfonic acid (HSMA), a product of the atmospheric oxidation of formaldehyde and considered a tracer for anthropogenic emissions. In contrast, there is no evidence for biomass burning influence on the filter sample from the 12th of November, which instead has an NMR spectral fingerprint more typical of background clean and marine influenced environments. It contains marine biogenic tracers like glycerol, methane-sulfonic acid (MSA), amines (DMA and TMA in particular) and alkylic chains, potentially attributable to lipids from marine biota. The presence of possible fatty acid alkylic chains, which were also observed on the 24th of December sample, and found by FIGAERO-CIMS in the cloud residuals, suggests that marine aerosol contributes to Arctic cloud formation, but this needs to be further investigated.

Future work will shed further light into the importance of the WBF process and SIP throughout the seasons. In addition, the role of particle and gas phase chemistry and the role of biological particles in cloud formation is being investigated.

b. Ice nucleating particle concentrations

INP measurements were conducted at the Swiss Site with HINC and DRINCZ, at the Zeppelin Observatory with CRAFT, and at Gruvebadet with DFPC. Despite the different techniques used, the INPCs as a function of temperature measured by the four methods agree within a factor of around 5 (Fig. 7). This is substantial for a highly spatiotemporally varying quantity such as INPs, which occur at very low concentrations. The observed INPC ranged from ~2 StdL^{-1} at -30°C down to the lowest detectable concentration of ~10^{-4} StdL^{-1} at -10°C. While there is agreement between the INPCs measured in the overlap temperature range (-21° to -15°C), on average the INPCs obtained at the Zeppelin Observatory are slightly below those measured at Gruvebadet and at the Swiss Site (Fig. 7). This is likely because the Zeppelin Observatory experiences less local influence from the the boundary layer and from the town of Ny-Ålesund (Platt et al. 2021) (see Figure 8a). Moreover, the CRAFT measurements represent the INPCs averaged over three days, while at the Swiss Site INPCs were measured at higher frequency (10 min to 40 min averages). The use of two different filter cutoff sizes (PM1 and PM10) gives some information about the size of

Accepted for publication in *Bulletin of the American Meteorological Society*. DOI 10.1175/BAMS-D-21-0034.1.

the INPs. At -18°C (-15°C) the INPC retrieved from the PM10 filter were 10% (50%) higher than the one retrieved from the PM1 filter (squares and circles in Figure 7). This difference suggests that the observed INPs at -15°C were larger than 1 μm and smaller than 10 μm whereas the observed INPs at -18°C were smaller than 1 μm. This size dependence is consistent with previous studies (e.g., Mason et al. 2016) and highlights the importance of supermicron aerosol on ice formation at temperatures above -15 C.

For the most part of the day, higher aerosol concentrations ≥ 0.5 μm were measured at the Swiss Site than at the Zeppelin Observatory and an inverse trend is observed at the two sites (Fig. 8a). Only between 0300 and 0600 UTC and from 2000 UTC onward do the aerosol concentrations follow the same trend. Previous field measurements have suggested that biological particles are a key source of INPs in the Arctic (e.g., Bigg and Leck 2001; Tobo et al. 2019; Hartmann et al. 2020). Therefore, the contribution of biological particles as INPs is investigated via the fluorescent aerosol concentration and fraction at the Swiss Site. As the fraction of fluorescent aerosol was not constant throughout the day, implies that the fluorescent particles did not always scale with aerosol concentrations ≥ 0.5 μm (Fig. 8b). Rather the fluorescent aerosol made up a variable subset of the total aerosol population ≥ 0.5 μm, which likely had a myriad of sources. However, consistent with previous observations, the INPC and activated fraction at -12°C, follow the same trend as fluorescent aerosol concentration (Fig. 8b). This relationship suggests a correlation between the fluorescent particle concentrations and the observed INPC and INP activated fraction and therefore, provides additional evidence that biological particles could play an essential role in controlling cloud phase in the Arctic. Further analysis will be conducted to determine if INPC parametrizations based on biological particles should be used to accurately represent ice formation in Arctic clouds (Burrows et al. 2022).

c. Cloud microphysical properties

Three flights into clouds were performed with HoloBalloon on 12 November 2019 (Fig. S3). Here we focus on the cloud microphysical measurements taken with HOLIMO3B on HoloBalloon and the cloud radar between 1445 and 1630 UTC (Fig. 9), together with the INP and CCN measurement to identify the processes responsible for ice crystal and cloud droplet formation.

During the entire flight, HOLIMO3B measured CDNCs between 5 and 15 cm^{-3} and a mean diameter of ~30 µm (Fig. 9c). Drizzle drops with diameter larger than 56 µm contributed to this large mean diameter (Fig. 9c,e). In comparison, continental clouds typically have higher CDNC (40-1000 cm^{-3}) and a smaller mean diameter (8 µm) (Lohmann et al. 2016). Aerosol particles with dry diameters larger than 70 nm measured by an Differential Mobility Particle Sizer (DMPS) at the Zeppelin Observatory were used as a proxy for the CCN concentration, following the method described by Koike et al. (2019). The estimated CCN concentration between 1000 and 1700 UTC was ~9 cm^{-3} (not shown) and was comparable to the CDNCs measured by HOLIMO3B. This indicates that the cloud droplet formation was limited by the CCN availability and is in accordance with previous studies showing that CDNC is sensitive to CCN concentration in aerosol-limited pristine regions (e.g., Reutter et al. 2009; Moore et al. 2013).

During the first part of the flight (1445-1545 UTC), the mean Doppler velocities at the altitude of HoloBalloon were rapidly varying with time, even though the reflectivities remained less variable and HoloBalloon flew approximately at a constant altitude (Fig. 9a,b). This indicates a turbulent atmosphere, which is in accordance with the observed veering of the wind near the altitude of HoloBalloon (Fig. S3). This turbulence and updrafts have favored the formation of the drizzle drops observed by HOLIMO3G (Fig. 9c,e) (Ramelli et al. 2021). During the second part of the flight (1545-1620 UTC), a fall streak pattern is visible in the increased reflectivity measured by the cloud radar ($\geq$ 10 dBZ). As these two periods are quite distinct from each other, we refer in the following to the *turbulent period* (1445-1545 UTC) and the *fall streak period* (1545-1620 UTC).

We consider the fall streak period in detail. HOLIMO3B measured an increase in total ICNC from below 0.5 L^{-1} up to 55 L^{-1} (Fig. 9d). Large ice crystals (diameters $\geq$ 106 μm) consisting of columns, frozen drops, and aged particles, as well as small pristine ice crystals (diameters $\leq$ 106 μm) contributed to this increase (Fig. 9e,f). Between 1600 - 1610 UTC, the concentration of small pristine ice crystals reached up to 40 L^{-1} and was greater than the concentration of larger ice crystals (Fig. 9e,f). Note that the influence from ice crystals from the ground (e.g. blowing snow) can be neglected as HoloBalloon flew up to ~700 m above the surface. A representative set of (hand-labelled) pictures of ice crystals contributing to the total ICNC as shown in Figure 9f are displayed in Figure 10. Whereas the large ice crystals likely originated from higher portion of the clouds, the small pristine ice crystals must have formed close to the measurement location of HoloBalloon, as ice crystals grow rapidly in the water saturated environment. In the temperature regime of the HoloBalloon measurements (between -8° and -1°C), the INPCs were below the instrument detection limit (no data in Fig. 7) and at cloud top temperatures (-13.5° to -11°C), the INPCs were on the order of $\sim 10^{-3}$ StdL^{-1}. As such, primary ice nucleation due to INPs acting in the immersion mode alone can neither explain the concentration of larger ice crystals originating from close to cloud top, nor the concentration of small ice crystals formed close to the measurement location of HoloBalloon. Therefore, we deduce that SIP enhanced the formation of the ice crystals in higher parts of the cloud and that SIP close to the measurement location was responsible for the sudden increase in concentration of small pristine ice crystals observed.

Our interpretation is that the primary ice was formed aloft where the cloud temperature was lower and thus more INPs were present. Then, SIP increased the ICNC near cloud top and the ice crystals grew until they were heavy enough to overcome the updrafts. As they fell, they continued to grow as columns (Fig. 10), consistent with the ambient temperature experienced, until they reached the altitude of HoloBalloon, as indicated by the higher radar reflectivities with decreasing altitude in the cloud (Fig. 9a). The columns then collided with drizzle drops, producing the observed ’ice lollipops’ (Fig. 10) consisting of frozen drizzle drops and columns (Keppas et al. 2017). Such ice lollipops were also observed by HOLIMO3G and the Hawkeye Probe at the Zeppelin Observatory (Fig. S6). Upon collision and freezing, the drizzle drops likely created splinters through droplet shattering (e.g., Lauber et al. 2018; Korolev and Leisner 2020). Laboratory experiments have shown that the number of ice splinters produced from a single drop freezing can reach up to 200 (Korolev and Leisner 2020). The splinters produced during the freezing of the drizzle drops then grew to the small columns observed by HOLIMO3B. These small columns could in turn collide with drizzle drops, initiate their freezing, and the formation of additional ice splinters. We suggest that this can lead to a cascading SIP process explaining the rapid increase in concentrations of small ice crystals observed, similarly to the study by Lawson et al. (2015).

Our findings on SIP are in agreement with other studies. First, the occurrence of SIP with low INPC (10^{-4} L^{-1} and 0.01 L^{-1}) was already observed in a study by Lawson et al. (2015). Second, a difference of up to four orders of magnitude between the INPC and ICNC are consistent with previous observations (e.g., Ladino et al. 2017; Li et al. 2021; Wieder et al. 2022a). Finally, a recent study using remote sensing techniques showed that droplet shattering was a more efficient SIP process than the rime-splintering process at slightly supercooled temperature in Arctic MPCs (Luke et al. 2021).

Next we demonstrate how the combination of the cloud radar and in-situ measurements complement each other to evaluate the microphysical properties of the observed MPC using the Passive and Active Microwave radiative TRAnsfer tool (PAMTRA, Mech et al. 2020). PAMTRA simulated the cloud radar Doppler spectra based on the ice crystal and cloud droplet size distributions measured by HOLIMO3B (Fig. 11). The variety of ice crystal habits were described by three categories (small ice, large ice, and frozen drops). More information about the PAMTRA settings is provided in the SI. Three representative time periods are compared (Fig. 11): (1) during the turbulent period (1525-1530 UTC) with cloud droplets, drizzle drops, and a low concentration of ice crystals, (2) during the fall streak period (1600-1605 UTC) with frozen drops and a higher concentration of ice crystals, and (3) during the period afterwards (1625-1630 UTC) with low concentration of cloud droplets and drizzle drops.

We start by allocating parts of the Doppler spectra signal to the different hydrometeor types. In the PAMTRA simulations, large ice crystals were generally responsible for the higher reflectivities (up to 5 dBZ) with fall velocities between 0-2.5 m s^{-1} (Fig. 11e,f). This is due to the strong dependence of reflectivity on particle size (Doviak and Zrnić 2006). Meanwhile, the measured frozen and drizzle drops were responsible for the simulated reflectivity at large fall velocities (up to 3 m s^{-1}) (Fig. 11e) and for the lower reflectivity (up to -20 dBZ) with fall velocities up to 2 m s^{-1} (Fig. 11d-f), respectively. Finally, measured cloud droplets and smaller ice crystals (diameter $\leq$ 100 μm) were only responsible for reflectivities below -30 and -80 dBZ, respectively, and fall velocities around 0 m s^{-1}.

Applying these results to the cloud radar measurements along the HoloBalloon path during the fall streak period (Fig. 9b), we find that the higher reflectivities with Doppler velocities of around 1 m s^{-1} (Fig. 9b) were produced by large falling ice crystals, whereas observed reflectivities below -40 dBZ and fall velocities between 2 and 4 m s^{-1} were generated by frozen drops, as only these particles have such high fall velocities and low reflectivity (Fig. 9b). The reflectivity between -30 and -10 dBZ at Doppler velocities around 0 m s^{-1} indicates the presence of small ice crystals, and possibly cloud droplets when reflectivities are at the lower side (below -17 dBz, (see e.g., Kogan et al. 2005)). Nevertheless, when looking at the PAMTRA simulations during the turbulent time periods, it can be difficult to distinguish the contributions of different hydrometeors to the Doppler spectra. Indeed, the reflectivity and fall velocity of drizzle drops and large ice crystals overlap and the drizzle drops are responsible for the highest reflectivities and fall velocities (Fig. 11d). The combination of the information obtained by HOLIMO3B and by the Doppler spectra is thus complementary and help to get a better understanding of the microphysical processes in Arctic MPCs.

d. Model comparison

To understand how the representation of clouds can be ameliorated in weather and climate models, we compared the cloud properties simulated by the regional WRF model with the in-situ cloud measurements. To represent the microphysics we used the double moment scheme developed by Milbrandt and Yau (2005), which has six classes for cloud water, ice, rain, snow, graupel and hail. The CCN concentration was prescribed as 9 cm^{-3} based on the concentration of aerosols > 70 nm (Koike et al. 2019)(Makoto et al, 2019) and the INPC was prescribed based on the exponential fit of the INPC measurements on 12 November shown in Figure 7. The simulated meteorological conditions were validated against the radiosonde observations (Fig. S7). Further information about the model setup is given in the SI.

The data were averaged for each flight time period to compare the observed and simulated cloud properties. Additionally, to match the acquisition by HOLIMO3B, the simulated cloud droplets and drizzle/rain drops were merged into one category to obtain the total LWC and liquid droplet number concentration (LDNC). The same was done for simulated small cloud ice and larger precipitating ice crystals (snow, hail, graupel) to obtain total ice water content (IWC) and ICNC.

The model correctly simulated an increase in the cloud top height from flight 1 to 3 as measured by the cloud radar (Fig. S9). Also, the cloud base height derived from the simulated hydrometeor populations follows the development indicated by the ceilometer measurements (Fig. S9). Hereafter we focus on flight 3, when HOLIMO3B observed substantial SIP to assess how well the model reproduces ice production in Arctic MPCs (Fig. 12). Generally, the simulation is in agreement with the observations as the LDNC and LWC are consistent with the maximum values measured by HOLIMO3B between 600 and 750 m a.s.l., albeit at altitudes between 1000 and 1500 m a.sl.. Below the simulated cloud base (~600 m a.sl.), the simulation underestimates the LDNC and LWC. This may be the reason for the sharper decrease in the simulated ICNC and IWC than in the observed ones below 300 m a.s.l.. Regardless, the simulation reproduces the maximum concentrations of ICNC and IWC observed by HOLIMO3B during flight 3, but the principle constituent of the simulated ICNC and IWC is graupel, which was not observed by HOLIMO3B (see Figs. 9f and 10). The ability for the simulation to reproduce the observed ICNC is surprising considering that the prescribed INPC at cloud top (~10^{-3} L^{-1}) is approximately four orders of magnitude lower than the observed and simulated ICNC. The Milbrandt and Yau scheme (Milbrandt and Yau 2005) includes SIP via the Hallett-Mossop (HM) process (Hallett and Mossop 1974), which could potentially improve the models ability to accurately predict the ICNC, especially as a significant fraction of the cloud falls within the temperature range relevant for the HM process (Fig. 12c,d). To determine if the HM process is responsible for the realistic ICNC simulated, we conducted the simulation again without the HM process activated. The ICNC decreases above ~800 m when the HM process is deactivated (Fig. 12). However, below this height, the model still simulates ICNCs that exceed the maximum ICNC when the HM process is active. This indicates that the microphysics scheme is producing ice independently of HM being active in the simulations. This may partly be due to the Milbrandt and Yau scheme lacking a sink term for INPC, which has been recommended to prevent models from nucleating ice continuously (Kärcher and Marcolli 2021). Regardless, the production of graupel by the model when none was actually observed, indicates that the simulations fail to

Accepted for publication in *Bulletin of the American Meteorological Society*. DOI 10.1175/BAMS-D-21-0034.1.

accurately represent the formation and evolution of ice in Arctic MPCs.

To conclude, the simulation is able to qualitatively represent the structure of the cloud, including the cloud top and base heights when the correct CCN and INP concentrations are prescribed. It also represents the realistic ICNC during flight 3 but for the wrong reasons. This indicates that the Milbrandt and Yau scheme has inconsistencies in the formation of ice hydrometeors and in particular, graupel, in the presence of very low CCN and INP concentrations representative of the Arctic. Future work will utilize the in-situ aerosol and cloud microphysical measurements as well as the remote sensing observations to address this inconsistency and develop and validate parametrizations for the SIP observed.

5. Summary and Future Work

The Ny-Ålesund Aerosol and Cloud Experiment (NASCENT) was initiated to improve our understanding on how aerosols, clouds, and their interactions influence the Arctic climate. A comprehensive set of cloud, aerosol, and meteorological observations was obtained over the course of one year, which included detailed in-situ and remote sensing techniques on ground-based and airborne platforms. Regarding the atmospheric seasonality, the mean temperature between December 2019 and April 2020 was substantially colder than the climatology (up to 6°C) due to a strong polar vortex, whereas the summer 2020 was slightly warmer than usual. The wind speed and direction was strongly influenced by the surrounding topography as found in previous studies. Aerosol particles, such as BC particles, followed the typical aerosol mass cycle found on Svalbard, with maximum concentrations during winter and spring. MPCs were the most abundant low cloud type during NASCENT. This high frequency highlights their importance for the Arctic climate.

We present first highlights from NASCENT by showing a detailed case study and discuss how in-situ observations of aerosols and clouds, together with remote sensing instrumentation and modelling can be combined to better understand the aerosol and cloud microphysical processes related to Arctic MPCs.

The cloud residuals measured by the CVI inlet were in good temporal agreement with measurements taken by two cloud probes at the Zeppelin Observatory. The measurements also revealed clear differences in molecular composition between ambient aerosol particles and those particles that were involved in cloud formation and evidence was found that biological particles acted as INP at warm temperatures. In future work, our dataset will be used to further examine the composition and physical properties of cloud residuals and ambient aerosols and their role and fate during cloud formation. Furthermore, a parametrization for estimating the INPC in the Arctic is under development.

Using aerosol in-situ measurements and vertical cloud profiling with the tethered balloon system HoloBalloon, we found that the cloud droplet formation was limited by the available CCN concentration. Regarding the cold cloud processes, we showed that INPC could not explain the measured ICNC. Instead, frozen drops, followed by an increase in small pristine ice crystals were observed and provide evidences for the occurrence of SIP via droplet shattering. Further measurements of the HoloBalloon system are being analyzed together with remote sensing observations to constrain the required conditions for different SIP processes in Arctic MPCs.

First modeling results with the WRF model have shown that the model is able to simulate the cloud structure and simulates a representative ICNC probably for the wrong reasons. In future work, more SIP parametrizations will be tested and compared to the measurements with HoloBalloon to ameliorate the representation of clouds in weather and climate models and to understand how they influence the radiative fluxes in the Arctic climate.

The NASCENT study has acquired a unique and holistic set of observations that will contribute to improve our understanding of aerosol and cloud processes in the Arctic. Together with further

Accepted for publication in *Bulletin of the American Meteorological Society*. DOI 10.1175/BAMS-D-21-0034.1.

in-depth analysis and modelling studies, this work will help to clarify their role in the observed Arctic Amplification and the Arctic climate system in general.

Acknowledgments. This project has received funding from the European Union's Horizon 2020 research and innovation programme under grant agreement No 821205 (FORCeS), from the Swiss Polar Institute (Exploratory Grants 2018), and from the Swiss National Science Foundation (SNSF) (grant no. 200021_175824). We gratefully acknowledge the funding by the European Research Council (ERC) (grant no. StG 758005) and the Deutsche Forschungsgemeinschaft (DFG, German Research Foundation) – Project-ID 268020496 – TRR 172, within the Transregional Collaborative Research Center "ArctiC Amplification: Climate Relevant Atmospheric and SurfaCe Processes, and Feedback Mechanisms (AC)^3". We are thankful for funding support from Knut and Alice Wallenberg (KAW) foundation financed projects Arctic Climate Across Scales (ACAS, project no. 2016.0024) and WAF project CLOUDFORM, grant no. 2017.0165, Swedish environmental protection agency (Naturvårdsverket), the Swedish Research Council (Vetenskapsrådet starting grant, project no. 2018-05045) and FORMAS agency funded project "Interplay between water vapor, clouds and aerosols in the Arctic". This project was supported by the Environment Research and Technology Development Fund (JPMEERF20202003) of the Environmental Restoration and Conservation Agency of Japan, and the Ministry of Education, Culture, Sports, Science, and Technology (MEXT) in Japan (ArCS II Project, JPMXD1420318865) and JSPS KAKENHI (grant numbers JP18H03745, JP18KK0292, JP19K14802, JP19H01972). This project was supported by the Korea Polar Research Institute (PE21010). We gratefully acknowledge funding from an access grant provided by the Research Council of Norway, project number 291644, Svalbard Integrated Arctic Earth Observing System – Knowledge Centre, operational phase. We thank Rafael Tazima (Brazil) for helping in designing our NASCENT logo of a polar bear studying the "nascency" of an Arctic cloud droplet. We thank Davide Ori for his precious help regarding the PAMTRA simulations. We owe great thanks to all technicians and helpers involved in the field work associated with NASCENT, particularly the AWIPEV and Norwegian Polar Institute Sverdrup stations staff.

Finally, we thank two anonymous reviewers for their constructive and helpful feedback on the manuscript, which strengthened the paper

Data availability statement. The data and meta-data of NASCENT study will be available on the Bolin Centre Data base (https://bolin.su.se/data/) using the keyword “NASCENT”. Data from AWIPEV is available in PANGAEA (www.pangaea.de). The Cloudnet dataset is available in the Cloudnet data portal (https://cloudnet.fmi.fi/).

Accepted for publication in *Bulletin of the American Meteorological Society*. DOI 10.1175/BAMS-D-21-0034.1.

References

Becagli, S., and Coauthors, 2019: Biogenic aerosol in the arctic from eight years of msa data from ny Ålesund (svalbard islands) and thule (greenland). *Atmosphere*, **10 (7)**, doi:10.3390/atmos10070349, URL https://www.mdpi.com/2073-4433/10/7/349.

Beck, A., J. Henneberger, J. P. Fugal, R. O. David, L. Lacher, and U. Lohmann, 2018: Impact of surface and near-surface processes on ice crystal concentrations measured at mountain-top research stations. *Atmospheric Chemistry and Physics*, **18 (12)**, 8909–8927, doi:10.5194/acp-18-8909-2018.

Beck, L. J., and Coauthors, 2020: Differing mechanisms of new particle formation at two arctic sites. *Geophysical Research Letters*, e2020GL091334.

Beine, H. J., S. Argentini, A. Maurizi, G. Mastrantonio, and A. Viola, 2001: The local wind field at Ny-Å lesund and the Zeppelin mountain at Svalbard. *Meteorology and Atmospheric Physics*, **78**, 107–113, doi:10.1007/s007030170009.

Bennartz, R., and Coauthors, 2013: July 2012 Greenland melt extent enhanced by low-level liquid clouds. *Nature*, **496 (83)**, doi:10.1038/nature12002.

Bergeron, T., 1935: On the physics of clouds and precipitation. *Report, International Union of Geodesy and Geophysics*, 156–180.

Bigg, E. K., and C. Leck, 2001: Cloud-active particles over the central arctic ocean. *Journal of Geophysical Research: Atmospheres*, **106 (D23)**, 32 155–32 166, doi:https://doi.org/10.1029/1999JD901152, URL https://agupubs.onlinelibrary.wiley.com/doi/abs/10.1029/1999JD901152, https://agupubs.onlinelibrary.wiley.com/doi/pdf/10.1029/1999JD901152.

Accepted for publication in *Bulletin of the American Meteorological Society*. DOI 10.1175/BAMS-D-21-0034.1.

Brean, J., M. Dall'Osto, R. Simó, Z. Shi, D. C. S. Beddows, and R. M. Harrison, 2021: Open ocean and coastal new particle formation from sulfuric acid and amines around the antarctic peninsula. *Nature Geoscience*, **14 (6)**, 383–388, doi:10.1038/s41561-021-00751-y, URL https://doi.org/10.1038/s41561-021-00751-y.

Burrows, S. M., and Coauthors, 2022: Ice-nucleating particles that impact clouds and climate: Observational and modeling research needs. *Reviews of Geophysics*, **60 (2)**, e2021RG000 745, doi:https://doi.org/10.1029/2021RG000745, URL https://agupubs.onlinelibrary.wiley.com/doi/abs/10.1029/2021RG000745, e2021RG000745 2021RG000745, https://agupubs.onlinelibrary.wiley.com/doi/pdf/10.1029/2021RG000745.

Choi, J. H., and Coauthors, 2019: Influence of biogenic organics on the chemical composition of arctic aerosols. *Global Biogeochemical Cycles*, **33 (10)**, 1238–1250, doi:https://doi.org/10.1029/2019GB006226, URL https://agupubs.onlinelibrary.wiley.com/doi/abs/10.1029/2019GB006226.

Cohen, J., and Coauthors, 2014: Recent arctic amplification and extreme mid-latitude weather. *Nature Geoscience*, **7 (9)**, 627–637, doi:10.1038/ngeo2234.

Curry, J. A., J. L. Schramm, W. B. Rossow, and D. Randall, 1996: Overview of Arctic Cloud and Radiation Characteristics. *Journal of Climate*, **9 (8)**, 1731–1764, doi:10.1175/1520-0442(1996)009<1731:OOACAR>2.0.CO;2.

Dahlke, S., and M. Maturilli, 2017: Contribution of atmospheric advection to the amplified winter warming in the arctic north atlantic region. *Advances in Meteorology*, **2017**, 4928 620, doi:10.1155/2017/4928620.

Dall'Osto, M., and Coauthors, 2017: Arctic sea ice melt leads to atmospheric new particle formation. *Scientific Reports*, **7**.

David, R. O., and Coauthors, 2019: Development of the droplet ice nuclei counter zurich (drincz): validation and application to field-collected snow samples. *Atmospheric Measurement Techniques*, **12 (12)**, 6865–6888, doi:10.5194/amt-12-6865-2019.

Dekhtyareva, A., K. Holmén, M. Maturilli, O. Hermansen, and R. Graversen, 2018: Effect of seasonal mesoscale and microscale meteorological conditions in Ny-Ålesund on results of monitoring of long-range transported pollution. *Polar Research*, **37 (1)**, 1508 196, doi:10.1080/17518369.2018.1508196, URL https://doi.org/10.1080/17518369.2018.1508196, publisher: Routledge _eprint: https://doi.org/10.1080/17518369.2018.1508196.

Deser, C., J. E. Walsh, and M. S. Timlin, 2000: Arctic sea ice variability in the context of recent atmospheric circulation trends. *Journal of Climate*, **13 (3)**, 617 – 633, doi:10.1175/1520-0442(2000)013<0617:ASIVIT>2.0.CO;2.

Dong, X., B. Xi, K. Crosby, C. N. Long, R. S. Stone, and M. D. Shupe, 2010: A 10 year climatology of Arctic cloud fraction and radiative forcing at Barrow, Alaska. *Journal of Geophysical Research: Atmospheres*, **115 (D17)**, doi:https://doi.org/10.1029/2009JD013489.

Doviak, R. J., and D. S. Zrnić, 2006: *Doppler radar and weather observations*. 3rd ed., Dover Publications, Inc.

Ebell, K., T. Nomokonova, M. Maturilli, and C. Ritter, 2020: Radiative Effect of Clouds at Ny-Ålesund, Svalbard, as Inferred from Ground-Based Remote Sensing Observations. *Journal of Applied Meteorology and Climatology*, **59 (1)**, 3–22, doi:10.1175/JAMC-D-19-0080.1.

Accepted for publication in *Bulletin of the American Meteorological Society*. DOI 10.1175/BAMS-D-21-0034.1.

Eleftheriadis, K., S. Vratolis, and S. Nyeki, 2009: Aerosol black carbon in the european arctic: Measurements at zeppelin station, ny-ålesund, svalbard from 1998–2007. *Geophys. Res. Lett.*, **36**, L02 809, doi:10.1029/2008GL035741.

Feltracco, M., and Coauthors, 2020: Interannual variability of sugars in arctic aerosol: Biomass burning and biogenic inputs. *Science of The Total Environment*, **706**, 136 089, doi:https://doi.org/10.1016/j.scitotenv.2019.136089, URL https://www.sciencedirect.com/science/article/pii/S0048969719360851.

Findeisen, W., 1938: Kolloid-meteorologische vorgänge bei neiderschlags-bildung. *Meteor. Z*, **55**, 121–133.

Freud, E., R. Krejci, P. Tunved, R. Leaitch, Q. T. Nguyen, A. Massling, H. Skov, and L. Barrie, 2017: Pan-arctic aerosol number size distributions: seasonality and transport patterns. *Atmos. Chem. Phys.*, **17 (13)**, 8101–8128, doi:10.5194/acp-17-8101-2017, URL https://www.atmos-chem-phys.net/17/8101/2017/.

Gierens, R., S. Kneifel, M. D. Shupe, K. Ebell, M. Maturilli, and U. Löhnert, 2020: Low-level mixed-phase clouds in a complex arctic environment. *Atmospheric Chemistry and Physics*, **20 (6)**, 3459–3481, doi:10.5194/acp-20-3459-2020.

Goosse, H., and Coauthors, 2018: Quantifying climate feedbacks in polar regions. *Nature communications*, **9 (1)**, 1–13.

Graversen, R. G., and M. Wang, 2009: Polar amplification in a coupled climate model with locked albedo. *Climate Dynamics*, **33 (5)**, 629–643, doi:10.1007/s00382-009-0535-6.

Hall, R. J., E. Hanna, and L. Chen, 2021: Winter arctic amplification at the synoptic timescale, 1979–2018, its regional variation and response to tropical and extratropical variability. *Climate Dynamics*, **56 (1)**, 457–473, doi:10.1007/s00382-020-05485-y.

Hallett, J., and S. C. Mossop, 1974: Production of secondary ice particles during the riming process. *Nature*, **249 (5452)**, 26–28, doi:10.1038/249026a0.

Harrington, J. Y., T. Reisin, W. R. Cotton, and S. M. Kreidenweis, 1999: Cloud resolving simulations of Arctic stratus: Part ii: Transition-season clouds. *Atmospheric Research*, **51 (1)**, 45 – 75, doi:10.1016/S0169-8095(98)00098-2.

Hartmann, M., and Coauthors, 2020: Wintertime airborne measurements of ice nucleating particles in the high arctic: A hint to a marine, biogenic source for ice nucleating particles. *Geophysical Research Letters*, **47 (13)**, e2020GL087 770, doi:https://doi.org/10.1029/2020GL087770, URL https://agupubs.onlinelibrary.wiley.com/doi/abs/10.1029/2020GL087770, e2020GL087770 10.1029/2020GL087770, https://agupubs.onlinelibrary.wiley.com/doi/pdf/10.1029/2020GL087770.

Heslin-Rees, D., M. Burgos, H.-C. Hansson, R. Krejci, J. Ström, P. Tunved, and P. Zieger, 2020: From a polar to a marine environment: has the changing arctic led to a shift in aerosol light scattering properties? *Atmospheric Chemistry and Physics*, **20 (21)**, 13 671–13 686, doi:10.5194/acp-20-13671-2020.

Illingworth, A. J., and Coauthors, 2007: Cloudnet: Continuous evaluation of cloud profiles in seven operational models using ground-based observations. *Bulletin of the American Meteorological Society*, **88 (6)**, 883 – 898, doi:10.1175/BAMS-88-6-883.

Accepted for publication in *Bulletin of the American Meteorological Society*. DOI 10.1175/BAMS-D-21-0034.1.

Kanji, Z. A., L. A. Ladino, H. Wex, Y. Boose, M. Burkert-Kohn, D. J. Cziczo, and M. Krämer, 2017: Overview of ice nucleating particles. *Meteorological Monographs*, **58**, 1.1 – 1.33, doi: 10.1175/AMSMONOGRAPHS-D-16-0006.1.

Kärcher, B., and C. Marcolli, 2021: Aerosol–cloud interactions: the representation of heterogeneous ice activation in cloud models. *Atmospheric Chemistry and Physics*, **21 (19)**, 15 213–15 220, doi:10.5194/acp-21-15213-2021, URL https://acp.copernicus.org/articles/21/15213/2021/.

Karlsson, L., R. Krejci, M. Koike, K. Ebell, and P. Zieger, 2021: A long-term study of cloud residuals from low-level arctic clouds. *Atmospheric Chemistry and Physics*, **21 (11)**, 8933–8959, doi:10.5194/acp-21-8933-2021, URL https://acp.copernicus.org/articles/21/8933/2021/.

Keppas, S. C., J. Crosier, T. W. Choularton, and K. N. Bower, 2017: Ice lollies: An ice particle generated in supercooled conveyor belts. *Geophysical Research Letters*, **44 (10)**, 5222–5230, doi:https://doi.org/10.1002/2017GL073441, URL https://agupubs.onlinelibrary.wiley.com/doi/abs/10.1002/2017GL073441, https://agupubs.onlinelibrary.wiley.com/doi/pdf/10.1002/2017GL073441.

Kogan, Z. N., D. B. Mechem, and Y. L. Kogan, 2005: Assessment of variability in continental low stratiform clouds based on observations of radar reflectivity. *Journal of Geophysical Research: Atmospheres*, **110 (D18)**, doi:https://doi.org/10.1029/2005JD006158, URL https://agupubs.onlinelibrary.wiley.com/doi/abs/10.1029/2005JD006158, https://agupubs.onlinelibrary.wiley.com/doi/pdf/10.1029/2005JD006158.

Koike, M., and Coauthors, 2019: Year-round in situ measurements of arctic low-level clouds: Microphysical properties and their relationships with aerosols. *Journal of Geophysical Research: Atmospheres*, **124 (3)**, 1798–1822, doi:10.1029/2018JD029802.

Kondo, Y., L. Sahu, N. Moteki, F. Khan, N. Takegawa, X. Liu, M. Koike, and T. Miyakawa, 2011: Consistency and traceability of black carbon measurements made by laser-induced incandescence, thermal-optical transmittance, and filter-based photo-absorption techniques. *Aerosol Science and Technology*, **45 (2)**, 295–312, doi:10.1080/02786826.2010.533215.

Korolev, A., 2007: Limitations of the Wegener–Bergeron–Findeisen Mechanism in the Evolution of Mixed-Phase Clouds. *Journal of the Atmospheric Sciences*, **64 (9)**, 3372–3375, doi:10.1175/JAS4035.1.

Korolev, A., and G. Isaac, 2003: Phase transformation of mixed-phase clouds. *Quarterly Journal of the Royal Meteorological Society*, **129 (587)**, 19–38, doi:10.1256/qj.01.203.

Korolev, A., and T. Leisner, 2020: Review of experimental studies on secondary ice production. *Atmospheric Chemistry and Physics Discussions*, **2020**, 1–42, doi:10.5194/acp-2020-537.

Korolev, A., and Coauthors, 2020: A new look at the environmental conditions favorable to secondary ice production. *Atmospheric Chemistry and Physics*, **20 (3)**, 1391–1429, doi:10.5194/acp-20-1391-2020.

Lacher, L., U. Lohmann, Y. Boose, A. Zipori, E. Herrmann, N. Bukowiecki, M. Steinbacher, and Z. A. Kanji, 2017: The horizontal ice nucleation chamber (hinc): Inp measurements at conditions relevant for mixed-phase clouds at the high altitude research station jungfraujoch. *Atmospheric Chemistry and Physics*, **17 (24)**, 15 199–15 224, doi:10.5194/acp-17-15199-2017.

Ladino, L. A., A. Korolev, I. Heckman, M. Wolde, A. M. Fridlind, and A. S. Ackerman, 2017: On the role of ice-nucleating aerosol in the formation of ice particles in tropical mesoscale convective systems. *Geophysical Research Letters*, **44 (3)**, 1574–1582, doi:https://doi.

org/10.1002/2016GL072455, URL https://agupubs.onlinelibrary.wiley.com/doi/abs/10.1002/2016GL072455, https://agupubs.onlinelibrary.wiley.com/doi/pdf/10.1002/2016GL072455.

Lauber, A., A. Kiselev, T. Pander, P. Handmann, and T. Leisner, 2018: Secondary Ice Formation during Freezing of Levitated Droplets. *Journal of the Atmospheric Sciences*, **75 (8)**, 2815–2826, doi:10.1175/JAS-D-18-0052.1.

Lawrence, Z. D., J. Perlwitz, A. H. Butler, G. L. Manney, P. A. Newman, S. H. Lee, and E. R. Nash, 2020: The remarkably strong arctic stratospheric polar vortex of winter 2020: Links to record-breaking arctic oscillation and ozone loss. *Journal of Geophysical Research: Atmospheres*, **125 (22)**, e2020JD033 271, doi:https://doi.org/10.1029/2020JD033271, e2020JD033271 10.1029/2020JD033271.

Lawson, R. P., S. Woods, and H. Morrison, 2015: The microphysics of ice and precipitation development in tropical cumulus clouds. *Journal of the Atmospheric Sciences*, **72 (6)**, 2429 – 2445, doi:10.1175/JAS-D-14-0274.1, URL https://journals.ametsoc.org/view/journals/atsc/72/6/jas-d-14-0274.1.xml.

Lee, H., and Coauthors, 2020a: Atmospheric new particle formation characteristics in the arctic as measured at mount zeppelin, svalbard, from 2016 to 2018. *Atmospheric Chemistry and Physics*, **20 (21)**, 13 425–13 441, doi:10.5194/acp-20-13425-2020, URL https://acp.copernicus.org/articles/20/13425/2020/.

Lee, S. H., Z. D. Lawrence, A. H. Butler, and A. Y. Karpechko, 2020b: Seasonal forecasts of the exceptional northern hemisphere winter of 2020. *Geophysical Research Letters*, **47 (21)**, e2020GL090 328, doi:https://doi.org/10.1029/2020GL090328, e2020GL090328 10.1029/2020GL090328.

Accepted for publication in *Bulletin of the American Meteorological Society*. DOI 10.1175/BAMS-D-21-0034.1.

Li, G., J. Wieder, J. T. Pasquier, J. Henneberger, and Z. A. Kanji, 2022: Predicting atmospheric background number concentration of ice nucleating particles in the arctic. *Atmospheric Chemistry and Physics Discussions*, **2022**, 1–27, doi:10.5194/acp-2022-21, URL https://acp.copernicus.org/preprints/acp-2022-21/.

Li, H., O. Möhler, T. Petäjä, and D. Moisseev, 2021: Multiyear statistics of columnar ice production in stratiform clouds over hyytiälä, finland. *Atmospheric Chemistry and Physics Discussions*, **2021**, 1–26, doi:10.5194/acp-2021-332, URL https://acp.copernicus.org/preprints/acp-2021-332/.

Lloyd, G., and Coauthors, 2015: Observations and comparisons of cloud microphysical properties in spring and summertime Arctic stratocumulus clouds during the ACCACIA campaign. *Atmospheric Chemistry and Physics*, **15 (7)**, 3719–3737, doi:10.5194/acp-15-3719-2015.

Lohmann, U., F. Lüönd, and F. Mahrt, 2016: *Clouds*, 1–25. Cambridge University Press, doi:10.1017/CBO9781139087513.002.

Luke, E. P., F. Yang, P. Kollias, A. M. Vogelmann, and M. Maahn, 2021: New insights into ice multiplication using remote-sensing observations of slightly supercooled mixed-phase clouds in the arctic. *Proceedings of the National Academy of Sciences*, **118 (13)**, doi:10.1073/pnas.2021387118.

Mason, R. H., and Coauthors, 2016: Size-resolved measurements of ice-nucleating particles at six locations in north america and one in europe. *Atmospheric Chemistry and Physics*, **16 (3)**, 1637–1651, doi:10.5194/acp-16-1637-2016, URL https://acp.copernicus.org/articles/16/1637/2016/.

Maturilli, M., 2020: Continuous meteorological observations at station Ny-Ålesund (2011-08 et seq). PANGAEA, URL https://doi.pangaea.de/10.1594/PANGAEA.914979.

Maturilli, M., A. Herber, and G. König-Langlo, 2013: Climatology and time series of surface meteorology in Ny-Ålesund, Svalbard. *Earth System Science Data*, **5 (1)**, 155–163, doi:10.5194/essd-5-155-2013.

Maturilli, M., A. Herber, and G. König-Langlo, 2013: Continuous meteorological observations at station Ny-Ålesund, 1993-08 to 2011-07. PANGAEA, URL https://doi.org/10.1594/PANGAEA.793046, doi:10.1594/PANGAEA.793046.

Maturilli, M., and K. Kayser, 2017: Arctic warming, moisture increase and circulation changes observed in the Ny-Ålesund homogenized radiosonde record. *Theoretical and Applied Climatology*, **130 (1-17)**, 1434–4483, doi:10.1007/s00704-016-1864-0.

McFarquhar, G. M., and Coauthors, 2011: Indirect and Semi-direct Aerosol Campaign. *Bulletin of the American Meteorological Society*, **92 (2)**, 183–201, doi:10.1175/2010BAMS2935.1.

Mech, M., M. Maahn, S. Kneifel, D. Ori, E. Orlandi, P. Kollias, V. Schemann, and S. Crewell, 2020: Pamtra 1.0: the passive and active microwave radiative transfer tool for simulating radiometer and radar measurements of the cloudy atmosphere. *Geoscientific Model Development*, **13 (9)**, 4229–4251, doi:10.5194/gmd-13-4229-2020.

Milbrandt, J., and M. Yau, 2005: A multimoment bulk microphysics parameterization. Part II: A proposed three-moment closure and scheme description. *Journal of Atmospheric Sciences*, **62 (9)**, 3065–3081.

Mioche, G., O. Jourdan, M. Ceccaldi, and J. Delanoë, 2015: Variability of mixed-phase clouds in the Arctic with a focus on the Svalbard region: a study based on spaceborne active remote sensing. *Atmospheric Chemistry and Physics*, **15 (5)**, 2445–2461, doi:10.5194/acp-15-2445-2015.

Moore, R. H., V. A. Karydis, S. L. Capps, T. L. Lathem, and A. Nenes, 2013: Droplet number uncertainties associated with ccn: an assessment using observations and a global model adjoint. *Atmospheric Chemistry and Physics*, **13 (8)**, 4235–4251, doi:10.5194/acp-13-4235-2013, URL https://acp.copernicus.org/articles/13/4235/2013/.

Morrison, H., G. de Boer, G. Feingold, J. Harrington, M. D. Shupe, and K. Sulia, 2011: Resilience of persistent Arctic mixed-phase clouds. *Nature Geoscience*, **5 (11)**, doi:10.1038/ngeo1332.

Nielsen, I. E., and Coauthors, 2019: Biogenic and anthropogenic sources of aerosols at the high arctic site villum research station. *Atmospheric Chemistry and Physics*, **19 (15)**, 10 239–10 256, doi:10.5194/acp-19-10239-2019, URL https://acp.copernicus.org/articles/19/10239/2019/.

Nomokonova, T., K. Ebell, U. Löhnert, M. Maturilli, C. Ritter, and E. O'Connor, 2019: Statistics on clouds and their relation to thermodynamic conditions at Ny-Ålesund using ground-based sensor synergy. *Atmospheric Chemistry and Physics*, **19 (6)**, 4105–4126, doi: 10.5194/acp-19-4105-2019.

Norwegian Polar Institute, 2014: Kartdata svalbard 1:100 000 (s100 kartdata) / map data. Norwegian Polar Institute, URL https://doi.org/10.21334/npolar.2014.645336c7, doi:10.21334/npolar.2014.645336c7.

Petzold, A., and M. Schönlinner, 2004: Multi-angle absorption photometry–a new method for the measurement of aerosol light absorption and atmospheric black carbon. *J. Aerosol Sci.*, **35 (4)**, 421–441.

Pithan, F., and T. Mauritsen, 2014: Arctic amplification dominated by temperature feedbacks in contemporary climate models. *Nature Geoscience*, **7 (3)**, 181–184, doi:10.1038/ngeo2071, URL https://doi.org/10.1038/ngeo2071.

Platt, S. M., and Coauthors, 2021: Atmospheric composition in the European Arctic and 30 years of the Zeppelin Observatory, Ny-Ålesund. *Atmospheric Chemistry and Physics Discussions*, 1–80, doi:10.5194/acp-2021-505, URL https://acp.copernicus.org/preprints/acp-2021-505/, publisher: Copernicus GmbH.

Quinn, P., G. Shaw, E. Andrews, E. Dutton, T. Ruoho-Airola, and S. Gong, 2007: Arctic haze: current trends and knowledge gaps. *Tellus B*, **59 (1)**, 99–114.

Ramelli, F., A. Beck, J. Henneberger, and U. Lohmann, 2020: Using a holographic imager on a tethered balloon system for microphysical observations of boundary layer clouds. *Atmospheric Measurement Techniques*, **13 (2)**, 925–939, doi:10.5194/amt-13-925-2020, URL https://amt.copernicus.org/articles/13/925/2020/.

Ramelli, F., and Coauthors, 2021: Influence of low-level blocking and turbulence on the microphysics of a mixed-phase cloud in an inner-alpine valley. *Atmospheric Chemistry and Physics*, **21 (6)**, 5151–5172, doi:10.5194/acp-21-5151-2021.

Rangno, A. L., and P. V. Hobbs, 2001: Ice particles in stratiform clouds in the Arctic and possible mechanisms for the production of high ice concentrations. *Journal of Geophysical Research: Atmospheres*, **106 (D14)**, 15 065–15 075, doi:10.1029/2000JD900286.

Reutter, P., and Coauthors, 2009: Aerosol- and updraft-limited regimes of cloud droplet formation: influence of particle number, size and hygroscopicity on the activation of cloud condensation nuclei (ccn). *Atmospheric Chemistry and Physics*, **9 (18)**, 7067–7080, doi:10.5194/acp-9-7067-2009, URL https://acp.copernicus.org/articles/9/7067/2009/.

Rinaldi, M., and Coauthors, 2017: Atmospheric ice nucleating particle measurements at the high mountain observatory mt. cimone (2165 m a.s.l., italy). *Atmospheric Environment*, **171**, 173–

180, doi:https://doi.org/10.1016/j.atmosenv.2017.10.027, URL https://www.sciencedirect.com/science/article/pii/S135223101730688X.

Santachiara, G., L. Di Matteo, F. Prodi, and F. Belosi, 2010: Atmospheric particles acting as ice forming nuclei in different size ranges. *Atmospheric Research*, **96 (2)**, 266–272, doi:https://doi.org/10.1016/j.atmosres.2009.08.004, URL https://www.sciencedirect.com/science/article/pii/S0169809509002361, 15th International Conference on Clouds and Precipitation.

Schacht, J., and Coauthors, 2019: The importance of the representation of air pollution emissions for the modeled distribution and radiative effects of black carbon in the Arctic. *Atmospheric Chemistry and Physics*, **19 (17)**, 11 159–11 183, doi:10.5194/acp-19-11159-2019, URL https://acp.copernicus.org/articles/19/11159/2019/.

Schmale, J., P. Zieger, and A. Ekman, 2021: Aerosols in current and future arctic climate. *Nat. Clim. Chang.*, **11**, 95–105, doi:10.1038/s41558-020-00969-5, URL https://doi.org/10.1038/s41558-020-00969-5.

Schmale, J., and Coauthors, 2019: Overview of the Antarctic Circumnavigation Expedition: Study of Preindustrial-like Aerosols and Their Climate Effects (ACE-SPACE). *Bulletin of the American Meteorological Society*, **100 (11)**, 2260–2283, doi:10.1175/BAMS-D-18-0187.1, URL https://journals.ametsoc.org/bams/article/100/11/2260/343773/Overview-of-the-Antarctic-Circumnavigation.

Schwarz, J. P., and Coauthors, 2006: Single-particle measurements of midlatitude black carbon and light-scattering aerosols from the boundary layer to the lower stratosphere. *Journal of Geophysical Research: Atmospheres*, **111 (D16)**, doi:10.1029/2006JD007076, URL https://agupubs.onlinelibrary.wiley.com/doi/10.1029/2006JD007076.

Sedlar, J., M. D. Shupe, and M. Tjernström, 2012: On the relationship between thermodynamic structure and cloud top, and its climate significance in the arctic. *Journal of Climate*, **25 (7)**, 2374 – 2393, doi:10.1175/JCLI-D-11-00186.1.

Shank, L. M., and Coauthors, 2012: Organic matter and non-refractory aerosol over the remote Southeast Pacific: oceanic and combustion sources. *Atmos. Chem. Phys.*, **12 (1)**, 557–576, doi:10.5194/acp-12-557-2012, URL http://www.atmos-chem-phys.net/12/557/2012/.

Shaw, G. E., 1995: The arctic haze phenomenon. *Bulletin of the American Meteorological Society*, **76 (12)**, 2403–2414.

Shupe, M. D., and J. M. Intrieri, 2004: Cloud Radiative Forcing of the Arctic Surface: The Influence of Cloud Properties, Surface Albedo, and Solar Zenith Angle. *Journal of Climate*, **17 (3)**, 616–628, doi:10.1175/1520-0442(2004)017<0616:CRFOTA>2.0.CO;2.

Sinha, P. R., and Coauthors, 2017: Evaluation of ground-based black carbon measurements by filter-based photometers at two arctic sites. *Journal of Geophysical Research: Atmospheres*, **122 (6)**, 3544–3572, doi:https://doi.org/10.1002/2016JD025843, URL https://agupubs.onlinelibrary.wiley.com/doi/abs/10.1002/2016JD025843.

Skamarock, W. C., and Coauthors, 2019: A description of the advanced research wrf model version 4. *National Center for Atmospheric Research: Boulder, CO, USA*, 145.

Stephens, M., N. Turner, and J. Sandberg, 2003: Particle identification by laser-induced incandescence in a solid-state laser cavity. *Applied Optics*, **42 (19)**, 3726, doi:10.1364/AO.42.003726, URL https://www.osapublishing.org/abstract.cfm?URI=ao-42-19-3726.

Stohl, A., 2006: Characteristics of atmospheric transport into the Arctic troposphere. *Journal of Geophysical Research: Atmospheres*, **111 (D11)**, doi:10.1029/

Accepted for publication in *Bulletin of the American Meteorological Society*. DOI 10.1175/BAMS-D-21-0034.1.

2005JD006888, URL https://agupubs.onlinelibrary.wiley.com/doi/abs/10.1029/2005JD006888, _eprint: https://agupubs.onlinelibrary.wiley.com/doi/pdf/10.1029/2005JD006888.

Stohl, A., and Coauthors, 2007: Arctic smoke — record high air pollution levels in the european arctic due to agricultural fires in eastern europe in spring 2006. *Atmospheric Chemistry and Physics*, **7 (2)**, 511–534, doi:10.5194/acp-7-511-2007, URL https://acp.copernicus.org/articles/7/511/2007/.

Ström, J., and Coauthors, 2003: One year of particle size distribution and aerosol chemical composition measurements at the Zeppelin Station, Svalbard, March 2000-March 2001. *Phys. Chem. Earth*, **28 (28-32)**, 1181–1190.

Sun, Z., and K. P. Shine, 1994: Studies of the radiative properties of ice and mixed-phase clouds. *Quarterly Journal of the Royal Meteorological Society*, **120 (515)**, 111–137, doi:10.1002/qj.49712051508.

Susskind, J., G. A. Schmidt, J. N. Lee, and L. Iredell, 2019: Recent global warming as confirmed by AIRS. *Environmental Research Letters*, **14 (4)**, 044 030, doi:10.1088/1748-9326/aafd4e.

Takahashi, T., Y. Nagao, and Y. Kushiyama, 1995: Possible high ice particle production during graupel–graupel collisions. *Journal of the Atmospheric Sciences*, **52 (24)**, 4523–4527, doi:10.1175/1520-0469(1995)052<4523:PHIPPD>2.0.CO;2.

Tjernström, M., and Coauthors, 2014: The Arctic Summer Cloud Ocean Study (ASCOS): overview and experimental design. *Atmospheric Chemistry and Physics*, **14 (6)**, 2823–2869, doi:10.5194/acp-14-2823-2014.

Tobo, Y., 2016: An improved approach for measuring immersion freezing in large droplets over a wide temperature range. *Scientific Reports*, **6 (1)**, 32 930, doi:10.1038/srep32930.

Tobo, Y., J. Uetake, H. Matsui, N. Moteki, Y. Uji, Y. Iwamoto, K. Miura, and R. Misumi, 2020: Seasonal trends of atmospheric ice nucleating particles over tokyo. *Journal of Geophysical Research: Atmospheres*, **125 (23)**, e2020JD033 658, doi:https://doi.org/10.1029/2020JD033658, e2020JD033658 2020JD033658-T.

Tobo, Y., and Coauthors, 2019: Glacially sourced dust as a potentially significant source of ice nucleating particles. *Nature Geoscience*, **12 (4)**, 253–258, doi:10.1038/s41561-019-0314-x.

Tunved, P., J. Ström, and R. Krejci, 2013: Arctic aerosol life cycle: linking aerosol size distributions observed between 2000 and 2010 with air mass transport and precipitation at zeppelin station, ny-Ã. . . lesund, svalbard. *Atmos. Chem. Phys.*, **13 (7)**, 3643–3660, doi:10.5194/acp-13-3643-2013, URL http://www.atmos-chem-phys.net/13/3643/2013/.

Turetta, C., M. Feltracco, E. Barbaro, A. Spolaor, C. Barbante, and A. Gambaro, 2021: A year-round measurement of water-soluble trace and rare earth elements in arctic aerosol: Possible inorganic tracers of specific events. *Atmosphere*, **12 (6)**, doi:10.3390/atmos12060694, URL https://www.mdpi.com/2073-4433/12/6/694.

Verheggen, B., and Coauthors, 2007: Aerosol partitioning between the interstitial and the condensed phase in mixed-phase clouds. *Journal of Geophysical Research: Atmospheres*, **112 (D23)**.

Wegener, A., 1911: Thermodynamik der atmosphäre. *Barth, Leipzig, Germany*.

Weinbruch, S., D. Wiesemann, M. Ebert, K. Schütze, R. Kallenborn, and J. Ström, 2012: Chemical composition and sources of aerosol particles at zeppelin mountain (ny ålesund, svalbard): An electron microscopy study. *Atmospheric Environment*, **49**, 142–150.

Wendisch, M., and Coauthors, 2017: Understanding causes and effects of rapid warming in the arctic. *EOS*, **98**, 22–26, doi:10.1029/2017EO064803.

Accepted for publication in *Bulletin of the American Meteorological Society*. DOI 10.1175/BAMS-D-21-0034.1.

Wendisch, M., and Coauthors, 2019: The Arctic Cloud Puzzle: Using ACLOUD/PASCAL Multiplatform Observations to Unravel the Role of Clouds and Aerosol Particles in Arctic Amplification. *Bulletin of the American Meteorological Society*, **100 (5)**, 841–871, doi: 10.1175/BAMS-D-18-0072.1.

Wieder, J., and Coauthors, 2022a: Retrieving ice nucleating particle concentration and ice multiplication factors using active remote sensing validated by in situ observations. *Atmospheric Chemistry and Physics Discussions*, **2022**, 1–47, doi:10.5194/acp-2022-67, URL https://acp.copernicus.org/preprints/acp-2022-67/.

Wieder, J., and Coauthors, 2022b: Unveiling atmospheric transport and mixing mechanisms of ice-nucleating particles over the alps. *Atmospheric Chemistry and Physics*, **22 (5)**, 3111–3130, doi:10.5194/acp-22-3111-2022, URL https://acp.copernicus.org/articles/22/3111/2022/.

Willis, M. D., W. R. Leaitch, and J. P. Abbatt, 2018: Processes controlling the composition and abundance of arctic aerosol. *Reviews of Geophysics*, **56 (4)**, 621–671.

Young, G., and Coauthors, 2016: Observed microphysical changes in Arctic mixed-phase clouds when transitioning from sea ice to open ocean. *Atmospheric Chemistry and Physics*, **16 (21)**, 13 945–13 967, doi:10.5194/acp-16-13945-2016.

Zangrando, R., E. Barbaro, P. Zennaro, S. Rossi, N. M. Kehrwald, J. Gabrieli, C. Barbante, and A. Gambaro, 2013: Molecular markers of biomass burning in arctic aerosols. *Environmental Science & Technology*, **47 (15)**, 8565–8574, doi:10.1021/es400125r, URL https://doi.org/10.1021/es400125r.

Zuidema, P., and Coauthors, 2005: An Arctic Springtime Mixed-Phase Cloudy Boundary Layer Observed during SHEBA. *Journal of the Atmospheric Sciences*, **62 (1)**, 160–176, doi:10.1175/

JAS-3368.1.

LIST OF TABLES

Accepted for publication in *Bulletin of the American Meteorological Society*. DOI 10.1175/BAMS-D-21-0034.1.

TABLE 1. List of abbreviations and acronyms

AA	Arctic Amplification
BC	Black Carbon
APS	Aerodynamic Particle Sizer
CCN	Cloud Condensation Nuclei
CCT	Climate Change Tower
CCNC	Cloud Condensation Nuclei Counter
CDNC	Cloud Droplet Number Concentration
CDP2	Cloud Droplet Probe
COSMOS	Continuous soot monitoring system
CPC	Condensation Particle Counter
CRAFT	Cryogenic Refrigerator Applied to Freezing Test
CVI	Counterflow Virtual Impactor
CPNC	Cloud particle number concentration
DFPC	Dynamic Filter Processing Chamber
DMA	Dimethylamine
DMPS	Differential Mobility Particle Size Spectrometer
DRINCZ	DRoplet Ice Nuclei Counter Zurich
eBC	equivalent Black Carbon
FIDAS	Fine Dust Measurement Device
FIGAERO-CIMS	iodide Chemical Ionization high-resolution time-of-flight Mass Spectrometer coupled to a Filter Inlet for Gases and AEROsols coupled to a Chemical Ionization Mass Spectrometer
Gly	glycerol
H-NMR	proton-Nuclear Magnetic Resonance spectroscopy
HMSA	Hydroxymethane-sulfonic acid
HINC	Horizontal Ice Nucleating Chamber
HOLIMO	HOlographic Imager for Microscopic Objects
ICNC	Ice Crystal Number Concentration
INP	Ice Nucleating Particle
INPC	Ice Nucleating Particles Concentration
IWC	Ice Water Content

L	levoglucosan
LDNC	Liquid droplet number concentration
LWC	Liquid Water Content
LWP	Liquid Water Path
MAAP	Multi-Angle Absorption Photometer
MBS	Multiparameter Bioaerosol Spectrometer
MPC	Mixed-Phase Clouds
MSA	Methane-Sulfonic Acid
NASCENT	Ny-Ålesund AeroSol Cloud ExperimeNT
OPC	Optical Particle Counter
p	Pressure
PAMTRA	The Passive and Active Microwave radiative TRAnsfer tool
PM1	Particulate Matter smaller 1 µm
PM10	Particulate Matter smaller 10 µm
PSAP	Particle Soot Absorption Photometer
rBC	refractory Black Carbon
RH	Relative Humidity
SIP	Secondary Ice Production
SI	Supplementary Information
SMPS	Scanning Mobility Particle Sizer
SP2-XR	extended-range Single-Particle Soot Photometer
T	Temperature
TMA	Trimethylamine
WBF	Wegener-Bergeron-Findeisen process
WIBS	Wideband Integrated Bioaerosol Sensor
WRF	Weather Research and Forecasting Model

TABLE 2. Retrieved variables at the five measurement locations. The black crosses show long-term measurements and the measurements performed only during NASCENT are represented with the symbol 'N'. Parameters that were in addition measured behind the ground-based Counterflow Virtual Impactor (CVI) inlet are marked by an asterisk (*).

	Measured quantities	*Zeppelin Obs.*	*HoloBalloon*	*Swiss Site*	*Gruvebadet*	*CCT*	*AWIPEV*
Meteorology	Wind vector	N	N	N		X	X
	Temperature	X	N	N	X	X	X
	RH	X		N	X	X	X
	Precipitation		N	N	X	X	X
	Vertical profiles of T, p, RH						X
	Vertical profiles wind vector					X	X
Cloud	Phase-resolved particle number size distribution	N	N				
	IWC	N	N				X
	LWC or LWP	N	N				X
	Ice crystal habits	N	N				
	Base & top height		N				X
	Radar reflectivity factor						X
Aerosol	Particle size distribution	X*		N	X		
	CCN properties	X*		N			
	INP concentration	X		N	X		
	Chemical composition	X/N*			N		
	Total particle concentration	X*			N		
	Particle size, shape, fluorescence	N*		N			
	Black carbon	X/N*			X		
	Single-particle analysis	X*					
Radiation	Broadband short-wave & longwave	X	N			X	X

LIST OF FIGURES

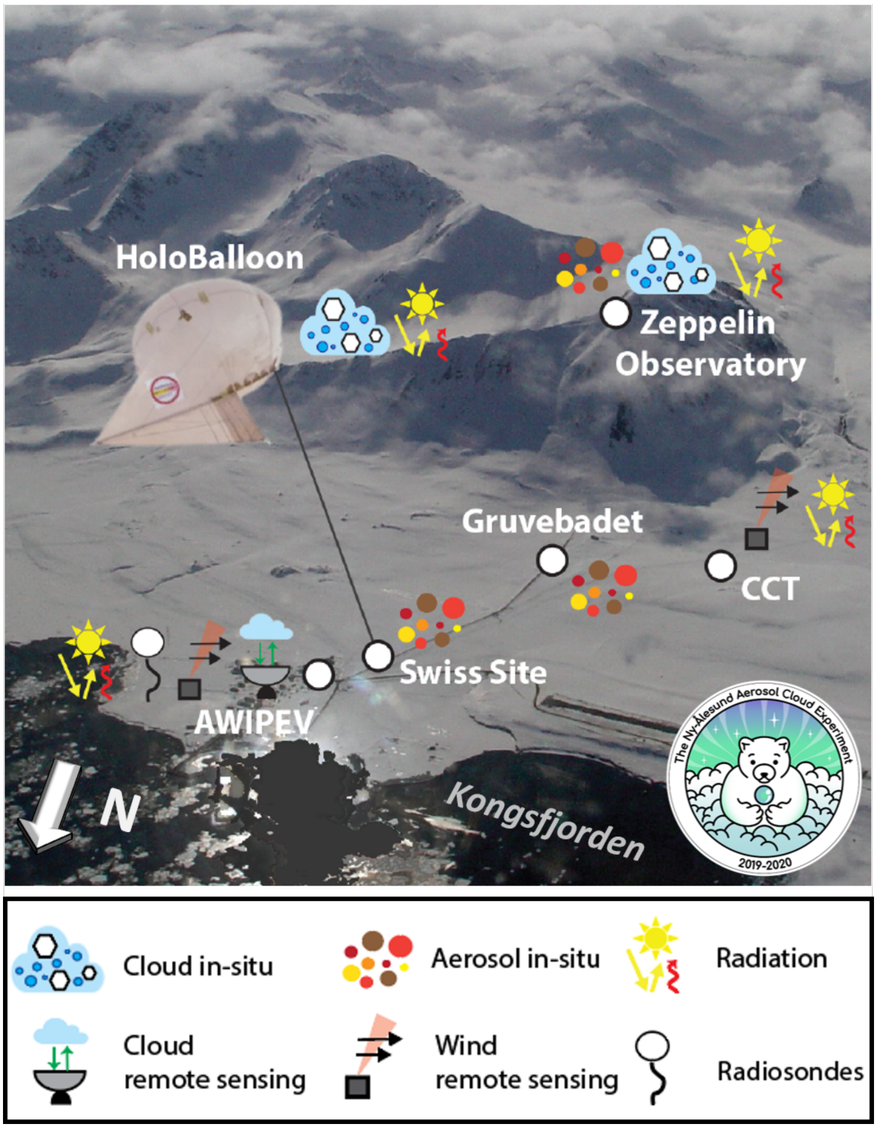

FIG. 1. Overview of the NASCENT study set-up at Ny-Ålesund, Svalbard. Aerial photo with the five measurement locations and the respective instrumentation. The campaign logo is shown in the lower right corner. Note that a topographic map with terrain contour is shown in Figure 4.

Accepted for publication in *Bulletin of the American Meteorological Society*. DOI 10.1175/BAMS-D-21-0034.1.

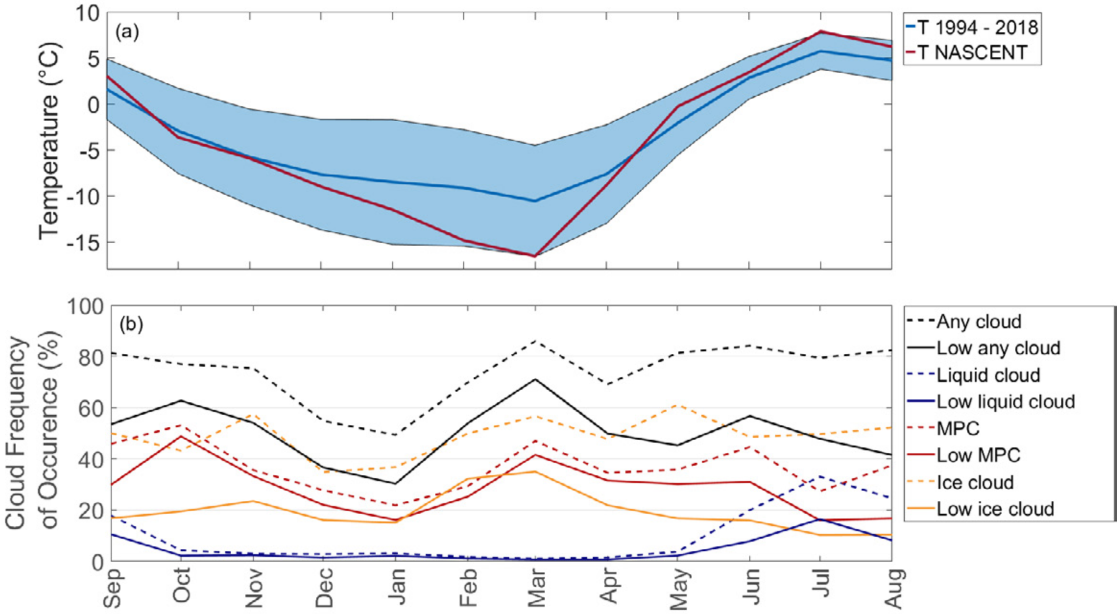

FIG. 2. Temperature and cloud seasonality observed during NASCENT. (a) Average temperatures during NASCENT compared to the climatology of 1994 to 2018 (shading represents the standard deviation) measured at the AWIPEV weather mast 10 m above ground (Maturilli et al. 2013). (b) Monthly frequency of occurrence of cloud types derived from the Cloudnet data during NASCENT. Colors represent the different cloud types, while dashed lines show all clouds in the column and solid lines the low-level clouds with cloud tops below three kilometers. Note that multiple cloud layers of different kinds are accounted for separately, so that the sum of 'liquid', 'ice', and 'mixed-phase' does not equal the frequency of 'any' clouds.

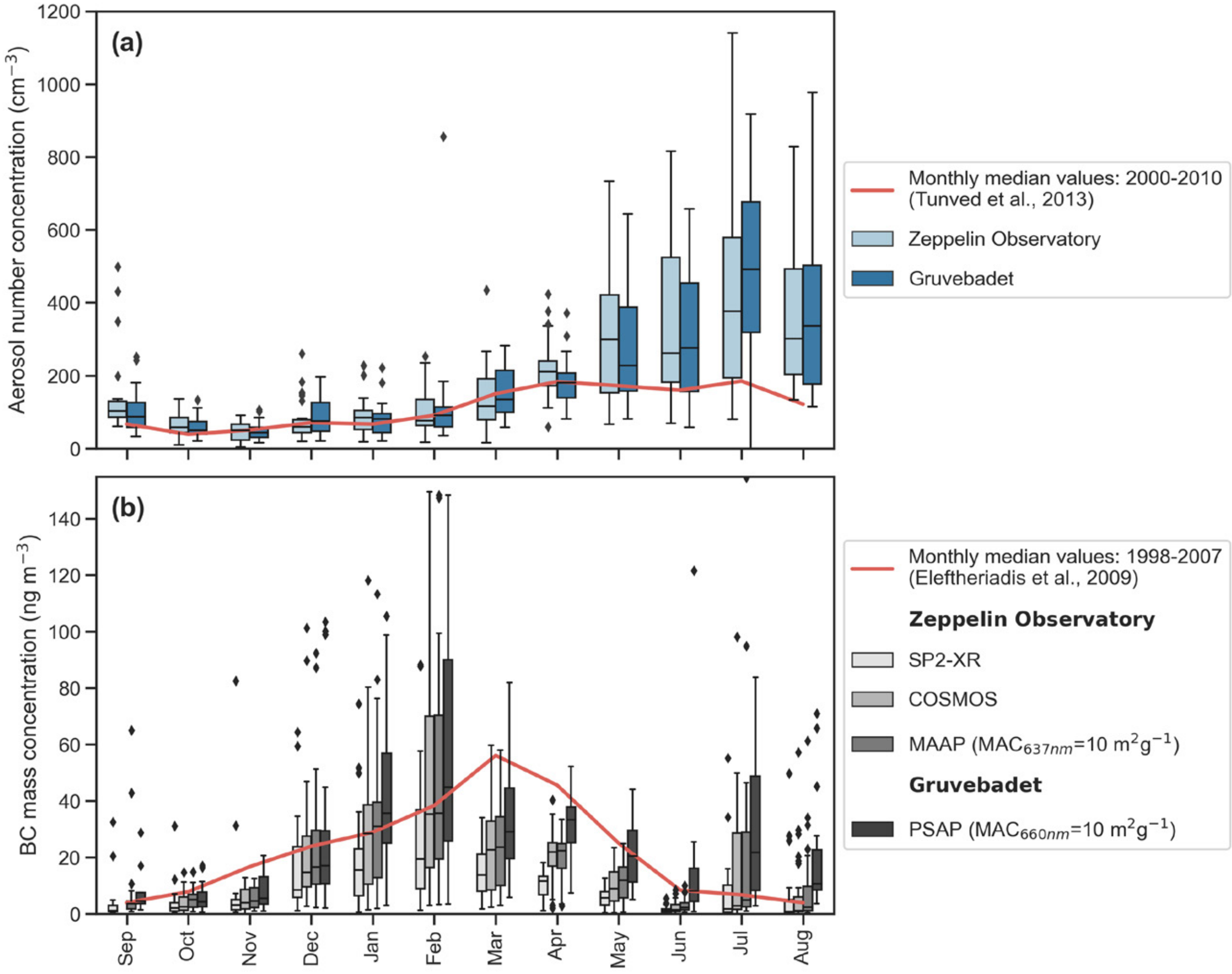

FIG. 3. Monthly average distributions of (a) aerosol particle number and (b) black carbon (BC) mass concentrations measured during NASCENT at Gruvebadet and at the Zeppelin Observatory in comparison to previous climatologies. The box-whisker plots show the quartiles and the 5th and 95th percentiles, respectively, while outliers are marked with diamonds. The particle number concentrations were measured using CPC's, while BC concentrations were measured by four different instruments: extended-range single-particle soot photometer (SP2-XR, Stephens et al. 2003; Schwarz et al. 2006), a multi-angle absorption photometer (MAAP, Petzold and Schönlinner 2004), a continuous soot monitoring system (COSMOS, Kondo et al. 2011), and a Particle Soot Absorption Photometer (PSAP).

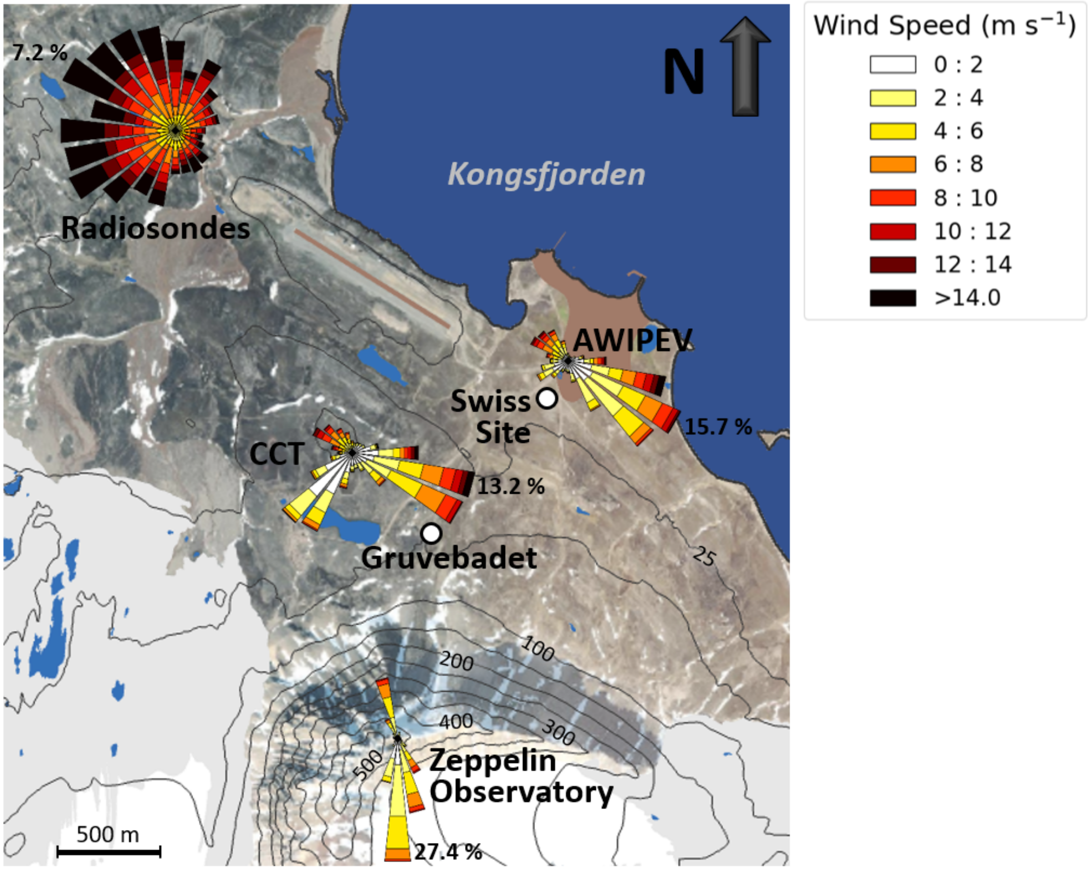

FIG. 4. Wind measurements during NASCENT throughout the Ny-Ålesund area at the different locations and retrieved from radiosondes. Data is shown for the AWIPEV weather mast (10 m), the Zeppelin Observatory, the CCT (10 m), and from daily radiosondes between 3000-3500 m a.s.l.. The bar length gives the respective frequency of occurrence with the maximum frequency value specified at the end of the longest bar. Topographic map of the Ny-Ålesund region from (Norwegian Polar Institute 2014).

Accepted for publication in *Bulletin of the American Meteorological Society*. DOI 10.1175/BAMS-D-21-0034.1.

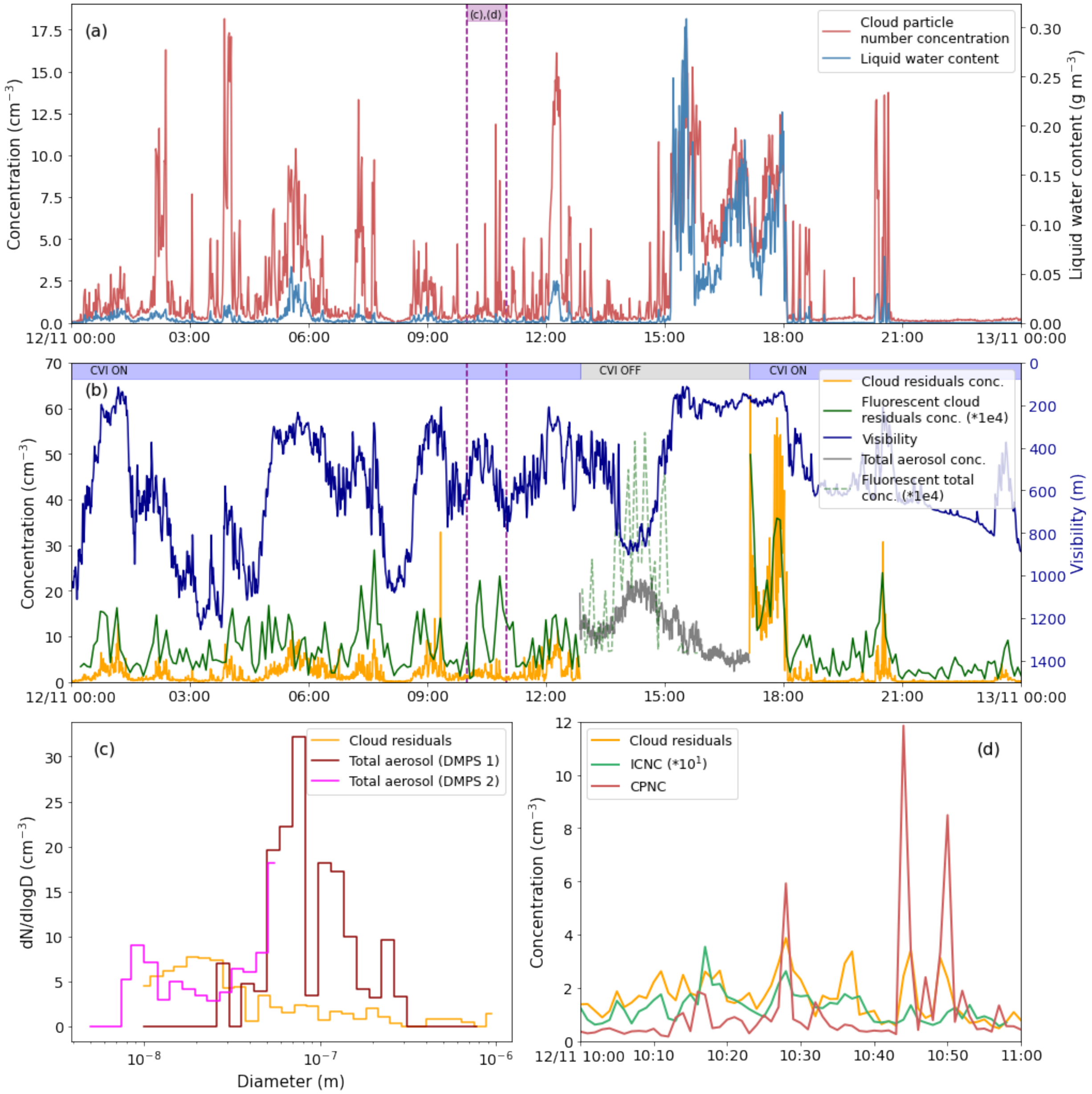

FIG. 5. Cloud in-situ measurements on 12 November 2019 at Zeppelin Observatory. (a) Cloud particle number concentration and liquid water content measured by the fog monitor. The period selected for the lower panels (c) and (d) is indicated. (b) Cloud residual number concentration and ambient aerosol number concentration, together with the fluorescent particle concentration (x 10^3) within the cloud residuals/ambient aerosol number concentrations, and ambient visibility measured at the CVI inlet (note the reversed y-axis). The shading at the top of the figure indicates when the CVI was in operation/ON. (c) Particle number size distribution of the cloud residuals and whole-air aerosols (interstitial and activated aerosol) measured by a tandem-DMPS system. (d) Cloud residual number concentration measured by the CVI inlet, ambient ICNC (x 10) measured by HOLIMO3G, and CPNC measured by the fog monitor.

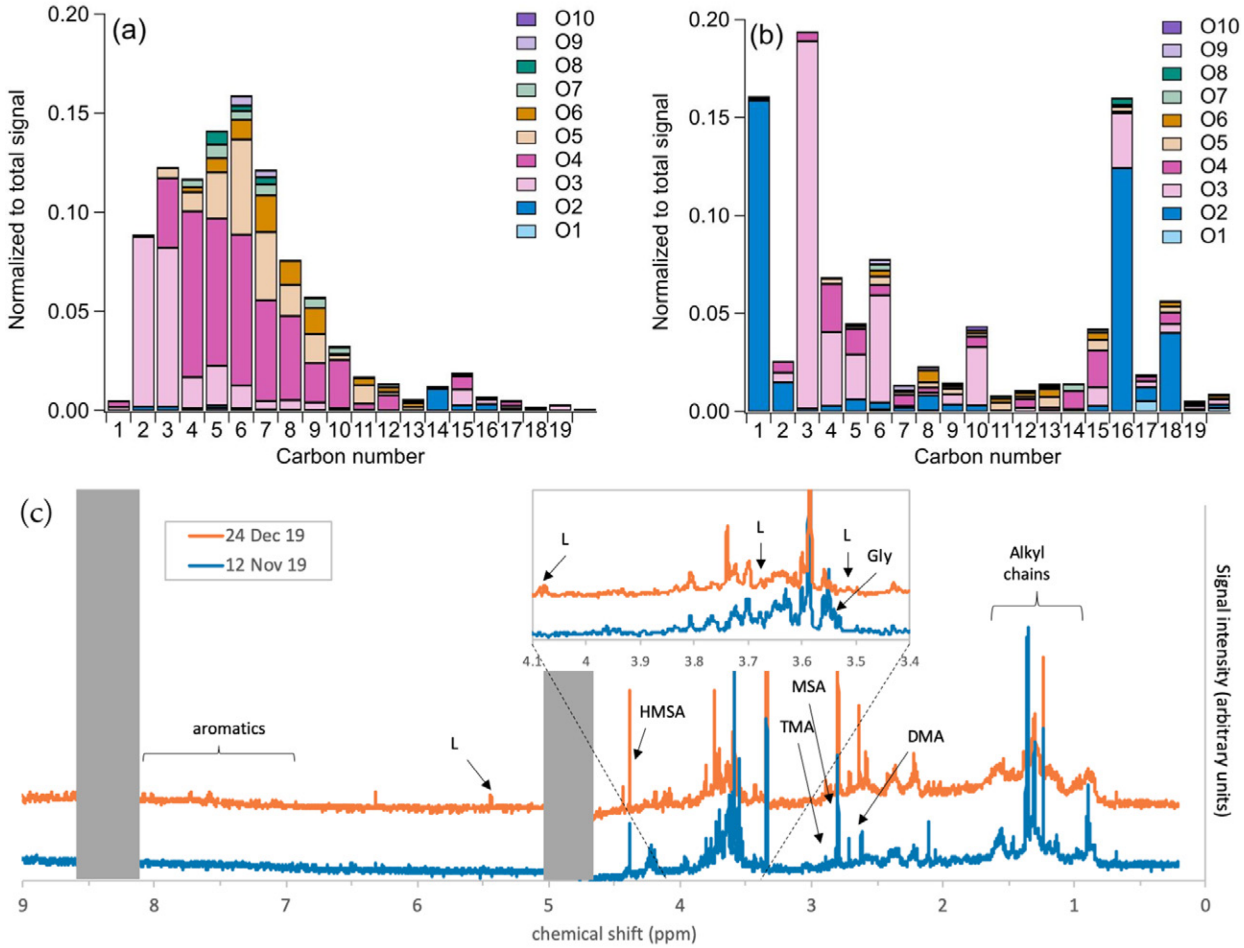

FIG. 6. High-resolution chemical composition of (a) aerosol particles before a cloud event (whole-air inlet) and (b) of cloud residuals during the cloud measured by the FIGAERO-CIMS on 24 December 2019. Shown is the background-corrected absolute signal of individual molecules, separated by the number of carbon and oxygen atoms. (c) ^{1}H-NMR spectra of ambient PM1 samples collected at Gruvebadet for 12 November and 24 December 2019. Specific resonances are assigned to levoglucosan (L), hydroxymethane-sulfonic acid (HMSA), methane-sulfonic acid (MSA), dimethylamine (DMA), trimethylamine (TMA) and glycerol (Gly). Unresolved mixtures of aromatic compounds and linear aliphatic chains, including possible contributions from lipids, are indicated in the spectra. The insert provides a focus on the aliphatic region of the spectra characteristic of polyols/saccarides compounds (H-C-O). Grey areas between 4.7 - 5.0 ppm and between 8 - 8.5 ppm cover the disturbance due to solvent and buffer solutions needed for the analysis.

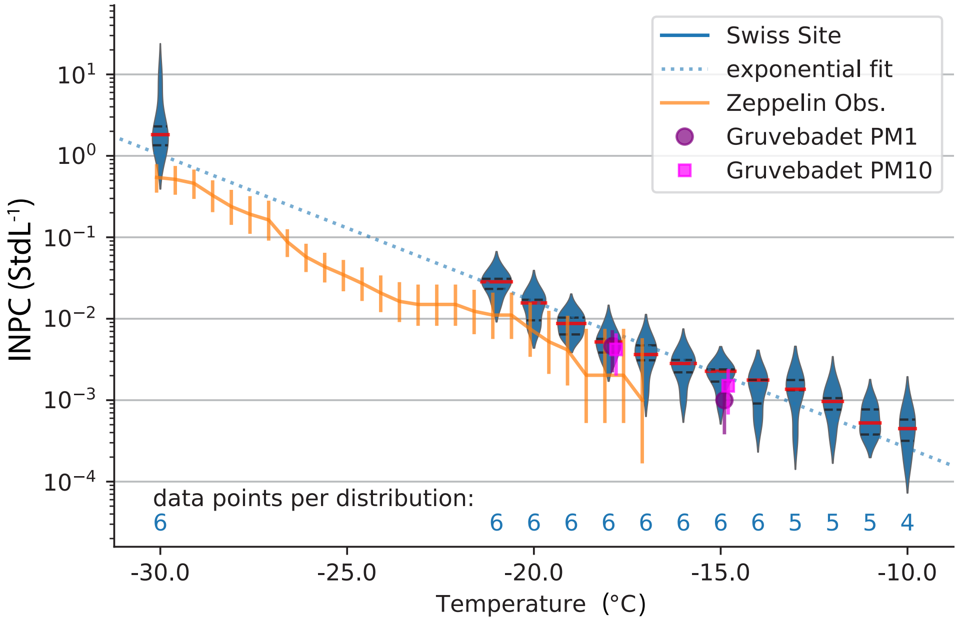

FIG. 7. Overview of INPCs observed on 12 November 2019. Blue violin plots: six INP samples measured with the DRoplet Ice Nuclei Counter Zurich (DRINCZ, David et al. 2019; Wieder et al. 2022b) between -10 °C and -21 °C and with the Horizontal Ice Nucleating Chamber (HINC, Lacher et al. 2017) at -30 °C at the Swiss Site. The red lines indicate the median and the dashed black lines the 25th and 75th percentiles. The blue dashed line shows the corresponding exponential fit ($INPC(T) = exp(-0.4146 \cdot T - 12.4059)$ (cf. Li et al. 2022)). Purple and Magenta: one filter sample collected between 0900 - 1200 UTC at Gruvebadet analyzed by the Dynamic Filter Processing Chamber (DFPC, Santachiara et al. 2010; Rinaldi et al. 2017) on PM1 and PM10. Orange line: one filter sample collected from 10 - 16 November 2019 at the Zeppelin Observatory analyzed by the Cryogenic Refrigerator Applied to Freezing Test (CRAFT, Tobo 2016; Tobo et al. 2019, 2020). The error bars represent the 95% confidence interval.

Accepted for publication in *Bulletin of the American Meteorological Society*. DOI 10.1175/BAMS-D-21-0034.1.

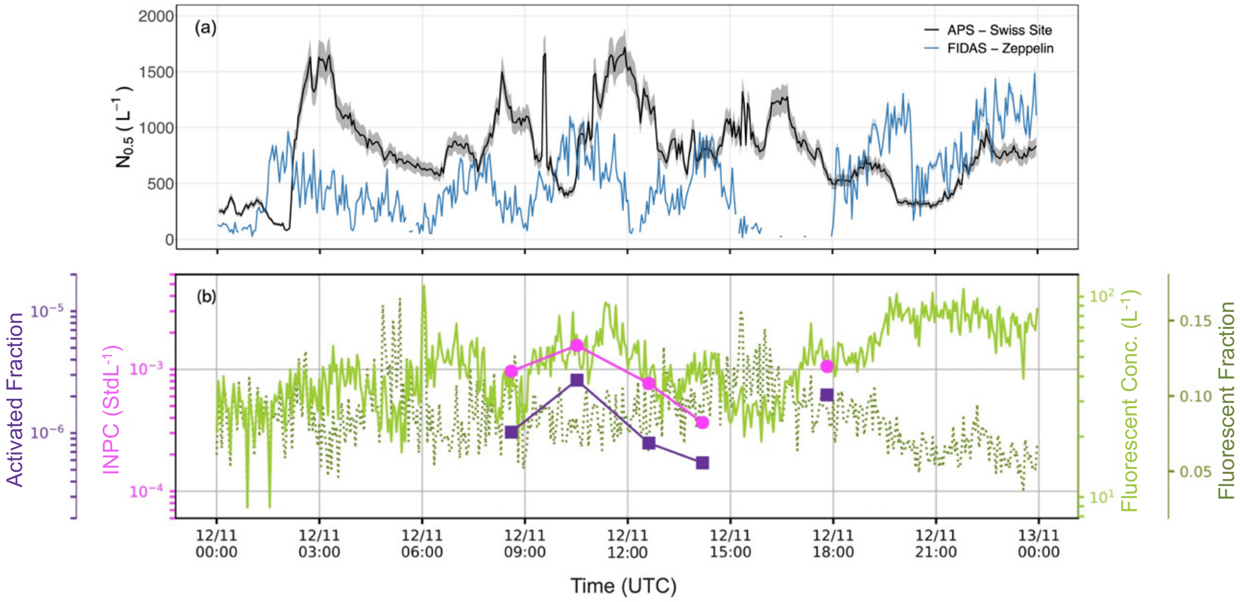

FIG. 8. (a) Particle number concentration for sizes ≥ 0.5 μm measured by the APS (aerodynamic diameter) at the Swiss Site and by the FIDAS (optical diameter) at the Zeppelin Observatory, with a time resolution of 3 minutes for both instruments. (b) INPC and activated fraction (INPC/$N_{0.5}$) at -12 °C (left axis), and fluorescent (particle) concentration and fluorescent (particle) fraction (right axis). We select a temperature of -12°C to adequately evaluate the contribution from biological aerosol particles (Kanji et al. 2017, and references therein). The INPCs are measured by DRINCZ and the fluorescent particle concentration by an Wideband Integrated Bioaerosol Sensor (WIBS). The fractions are normalized to the particle fraction ≥ 0.5 μm.

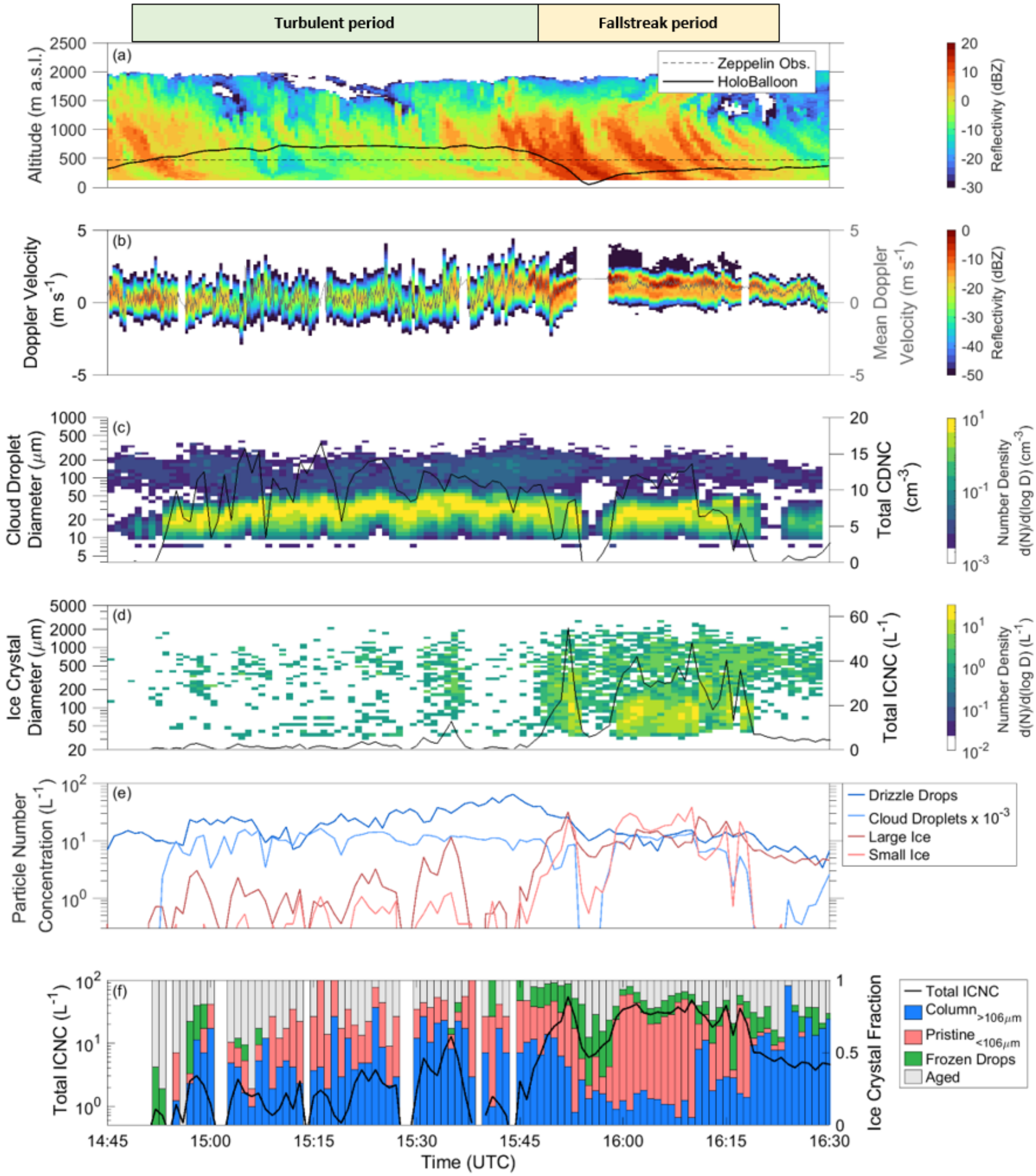
Turbulent period
Fallstreak period
(a)
Altitude (m a.s.l.)
2500
2000
1500
1000
500
0
Zeppelin Obs.
HoloBalloon
Reflectivity (dBZ)
20
10
0
-10
-20
-30
(b)
Doppler Velocity (m s^{-1})
5
0
-5
Mean Doppler Velocity (m s^{-1})
Reflectivity (dBZ)
0
-10
-20
-30
-40
-50
(c)
Cloud Droplet Diameter (μm)
1000
500
200
100
50
20
10
5
Total CDNC (cm^{-3})
20
15
10
5
0
Number Density d(N)/d(log D) (cm^{-3})
10^{1}
10^{-1}
10^{-3}
(d)
Ice Crystal Diameter (μm)
5000
2000
1000
500
200
100
50
20
Total ICNC (L^{-1})
60
40
20
0
Number Density d(N)/d(log D) (L^{-1})
10^{1}
10^{0}
10^{-1}
10^{-2}
(e)
Particle Number Concentration (L^{-1})
10^{2}
10^{1}
10^{0}
Drizzle Drops
Cloud Droplets x 10^{-3}
Large Ice
Small Ice
(f)
Total ICNC (L^{-1})
10^{2}
10^{1}
10^{0}
Ice Crystal Fraction
1
0.5
0
Total ICNC
Column$_{>106\mu m}$
Pristine$_{<106\mu m}$
Frozen Drops
Aged
14:45
15:00
15:15
15:30
15:45
16:00
16:15
16:30
Time (UTC)

FIG. 9. Overview of the cloud properties observed in-situ on HoloBalloon and by the cloud radar on 12 November 2019. (a) Cloud radar reflectivity, HoloBalloon path and Zeppelin altitude. (b) Doppler spectra and mean Doppler velocity at the height of the HoloBalloon path. Positive values represent a downward velocity. (c) Cloud droplet and (d) ice crystal size distributions (color) and total CDNC and ICNC (black line) measured by HOLIMO3B. (e) Cloud droplets, drizzle drops, and ICNC for crystals smaller and larger than 106 μm. This cut-off size is defined by the bin size closest to 100 μm. (f) Frequency of occurrence of the ice crystal habits and total ICNC. The data are averaged over 60 sec. Note that at around 1550 UTC, HoloBalloon flew out of the cloud, which explains the decrease in CDNC and ICNC measured by HOLIMO3B (c-f) and the missing reflectivity data at the HoloBalloon height (b).

Accepted for publication in *Bulletin of the American Meteorological Society*. DOI 10.1175/BAMS-D-21-0034.1.

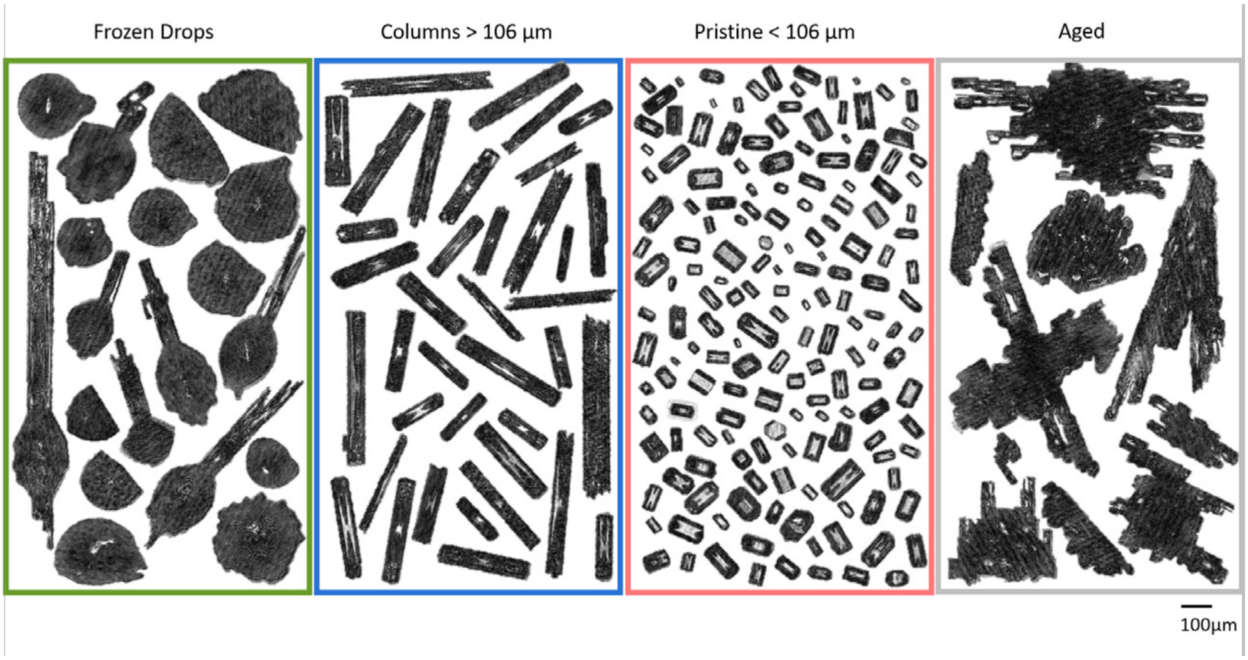

FIG. 10. Examples of ice crystals classified as typical habits observed with HOLIMO3B. Plates and (hollow) columns with a diameter smaller than 106 µm were classified as pristine, whereas larger columns were classified separately. Droplet 'lollipop', and drops showing evidence of freezing are classified as frozen drops. All the other ice crystals, including rimed and aggregated particles are classified as 'Aged'. The scale bar in the right panel is representative for all of the panels. The respective fractions of the typical ice crystals habits to the total ICNC are displayed in Figure 9f.

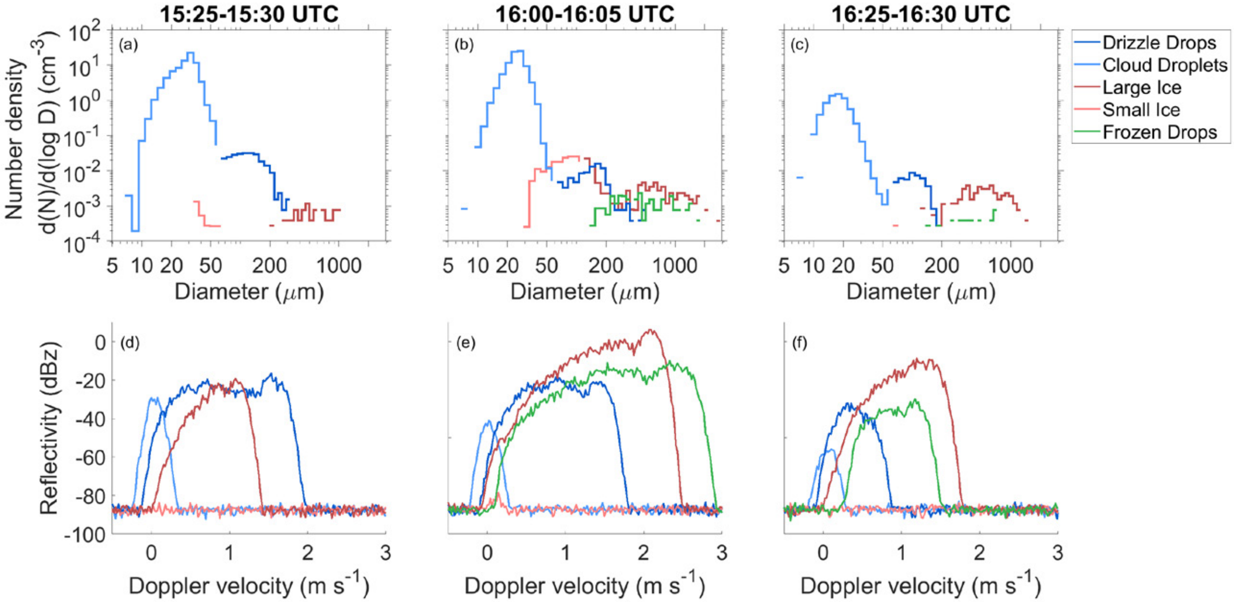

FIG. 11. (a-c) Measured size distributions from HOLIMO3B. (d-f) Radar Doppler spectra simulated with the PAMTRA tool using the size distribution shown in a-c. The measured size distribution and simulated Doppler spectra are shown at three characteristic time periods of 5 minutes: 1525-1530 UTC (a & d), 1600-1605 UTC (b & e), and 1625-1630 UTC (c & f).

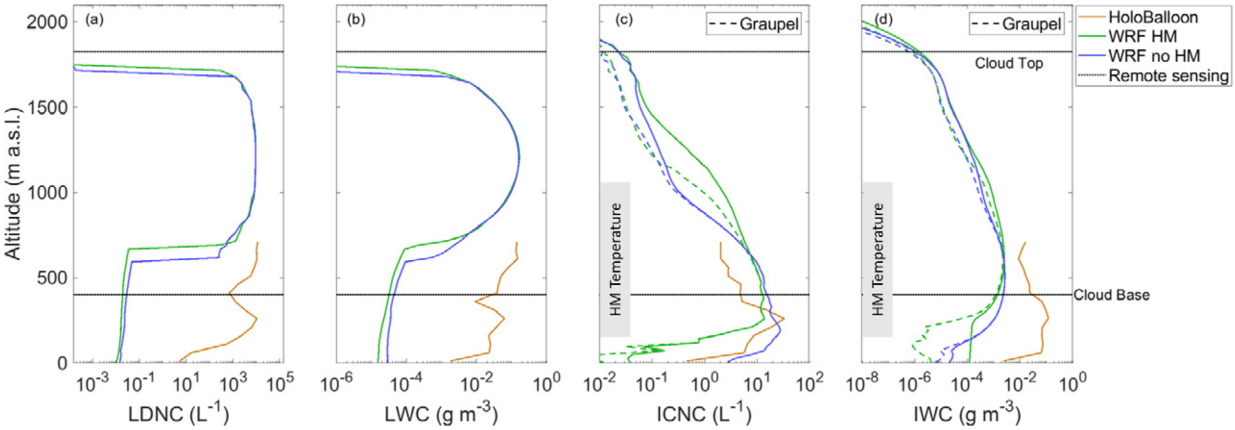

FIG. 12. The averaged vertical profiles during flight 3 on 12 November 2019 observed by HOLIMO3B and simulated by WRF. (a) LDNC, (b) LWC, (c) ICNC & (d) IWC. The contribution of graupel to the ICNC and IWC are shown with the colored dashed profile line in (c) and (d).The data from HOLIMO3B are averaged over 50 m altitude bins and the WRF data over every model layer. The average cloud base and cloud top measured by the remote sensing instrumentation (ceilometer and cloud radar, respectively) are represented by the black dotted horizontal lines and the HM temperature range (-8° to -3°C) is highlighted in (c) and (d).

Supplementary Material: The Ny-Ålesund Aerosol Cloud Experiment (NASCENT)

J. T. Pasquier* (1) and R. O. David (2) and G. Freitas (3,4) and R. Gierens (5) and Y. Gramlich (3,4) and S. Haslett (3,4) and G. Li (1) and B. Schäfer (2) and K. Siegel (3,4) and J. Wieder (1) and K. Adachi (17) and F. Belosi (14) and T. Carlsen (2) and S. Decesari (14) and K. Ebell (5) and S. Gilardoni (12,13) and M. Gysel-Beer (9) and J. Henneberger (1) and J. Inoue (6) and Z. A. Kanji (1) and M. Koike (7) and Y. Kondo (6) and R. Krejci (3,4) and U. Lohmann (1) and M. Maturilli (10) and M. Mazzolla (12,13) and R. Modini (9) and C. Mohr (3) and G. Motos (11) and A. Nenes (11, 19) and A. Nicosia (14) and S. Ohata (15, 16) and M. Paglione (14) and S. Park (8) and R. E. Pileci (9,21) and F. Ramelli (1) and M. Rinaldi (14) and C. Ritter (10) and K. Sato (18) and T. Storelvmo (2) and Y. Tobo (6) and and R. Traversi (20) and A. Viola (12,13) and P. Zieger† (3,4)

(1) Institute for Atmospheric and Climate Science, ETH Zürich, Zurich, Switzerland

(2) Department of Geosciences, University of Oslo, Oslo, Norway

(3) Department of Environmental Science, Stockholm University, Sweden

(4) Bolin Centre for Climate Research, Stockholm University, Sweden

(5) Institute for Geophysics and Meteorology, University of Cologne, Cologne, Germany

(6) National Institute of Polar Research (NIPR), Tachikawa, Tokyo, Japan

(7) Department of Earth and Planetary Science, Graduate School of Science, University of Tokyo, Tokyo, Japan

(8) Korea Polar Research Institute (KOPRI), Incheon, Korea

Early Online Release: This preliminary version has been accepted for publication in *Bulletin of the American Meteorological Society*, may be fully cited, and has been assigned DOI 10.1175/BAMS-D-21-0034.1. The final typeset copyedited article will replace the EOR at the above DOI when it is published.

(9) Laboratory of Atmospheric Chemistry, Paul Scherrer Institute (PSI), Villigen PSI, Switzerland

(10) Alfred Wegener Institute, Helmholtz Centre for Polar and Marine Research (AWI), Potsdam, Germany

(11) Laboratory of Atmospheric Processes and their Impacts, Ecole Polytechnique Fédérale de Lausanne, Lausanne, Switzerland

(12) Institute for Polar Sciences, CNR, Bologna, Italy

(13) Institute for Polar Sciences , CNR, Rome, Italy

(14) National Research Council, Institute of Atmospheric Sciences and Climate, CNR-ISAC, Bologna, Italy

(15) Institute for Space–Earth Environmental Research, Nagoya University, Nagoya, Aichi, Japan

(16) Institute for Advanced Research, Nagoya University, Nagoya, Aichi, Japan

(17) Meteorological Research Institute, Tsukuba, Ibaraki, Japan

(18) Kitami Institute of Technology, Kitami, Hokkaido, Japan

(19) Center for Studies of Air Quality and Climate Change, Institute for Chemical Engineering Sciences, Foundation for Research and Technology Hellas, Patras, Greece,

(20) Department of Chemistry, University of Florence, Florence, Italy

(21) U-Earth Biotech Ltd, London, United Kingdom

**Corresponding author*: Julie T. Pasquier, julie.pasquier@env.ethz.ch

†*Corresponding author*: Paul Zieger, paul.zieger@aces.su.se

In this supplementary material, we shortly describe the atmospheric situation on 12 November 2019 in Ny-Ålesund, Svalbard (Fig. S1), as mainly measurements taken this day are discussed in the main manuscript. Additionally, the major instrumentation used in this manuscript or installed in the framework of the Ny-Ålesund Aerosol Cloud Experiment (NASCENT) at the Swiss Site, the Zeppelin Observatory, Gruvebadet, the Climate Change Tower, and AWIPEV are described. Summarizing tables with the instrument parameters and availability are included. Finally, information about the WRF model setup are given, together with a short description of the simulation during flights 2 and 3 of HoloBalloon on 12 November 2019.

S1. Meteorological situation on 12 November 2019

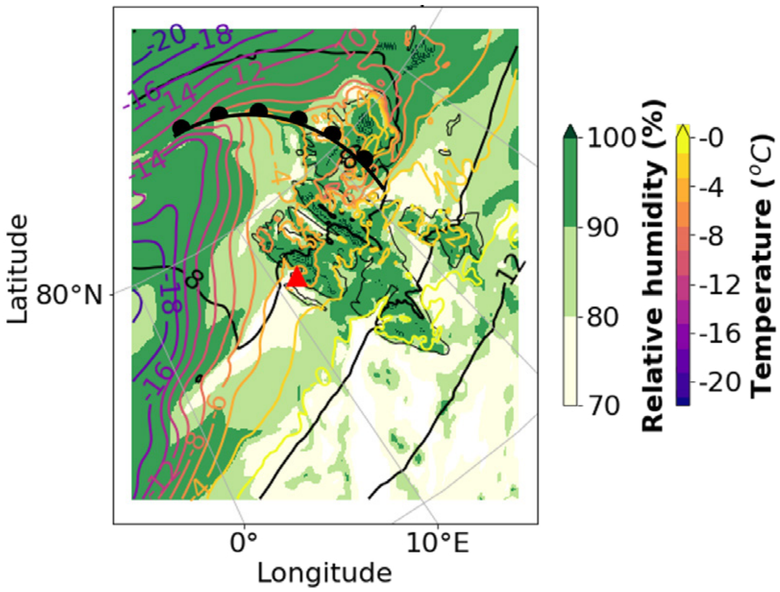

FIG. S1. Weathermap showing the relative humidity (green shading), temperature (colored lines) at 1000 hPa and the estimated location of the warm front at 0600 UTC on 12 November. The red triangle shows the location of Ny-Ålesund. The model data are from the MEPS Weathermaps Hellmuth and Hofer (2019).

A warm front passed over Ny-Ålesund on 11 November 2019. One day later, on 12 November 2019, Ny-Ålesund was located in the warm sector behind the warm front (Fig. S1). The temperature at the ground was therefore relatively high (varying between 0°C and -3°C and the pressure slightly increased from 1009 to 1011 hPa (not shown). Note that on this day the sun was permanently below the horizon with a minimum altitude of -29° and a maximum altitude of -7°. Thus no direct sunlight was shining.

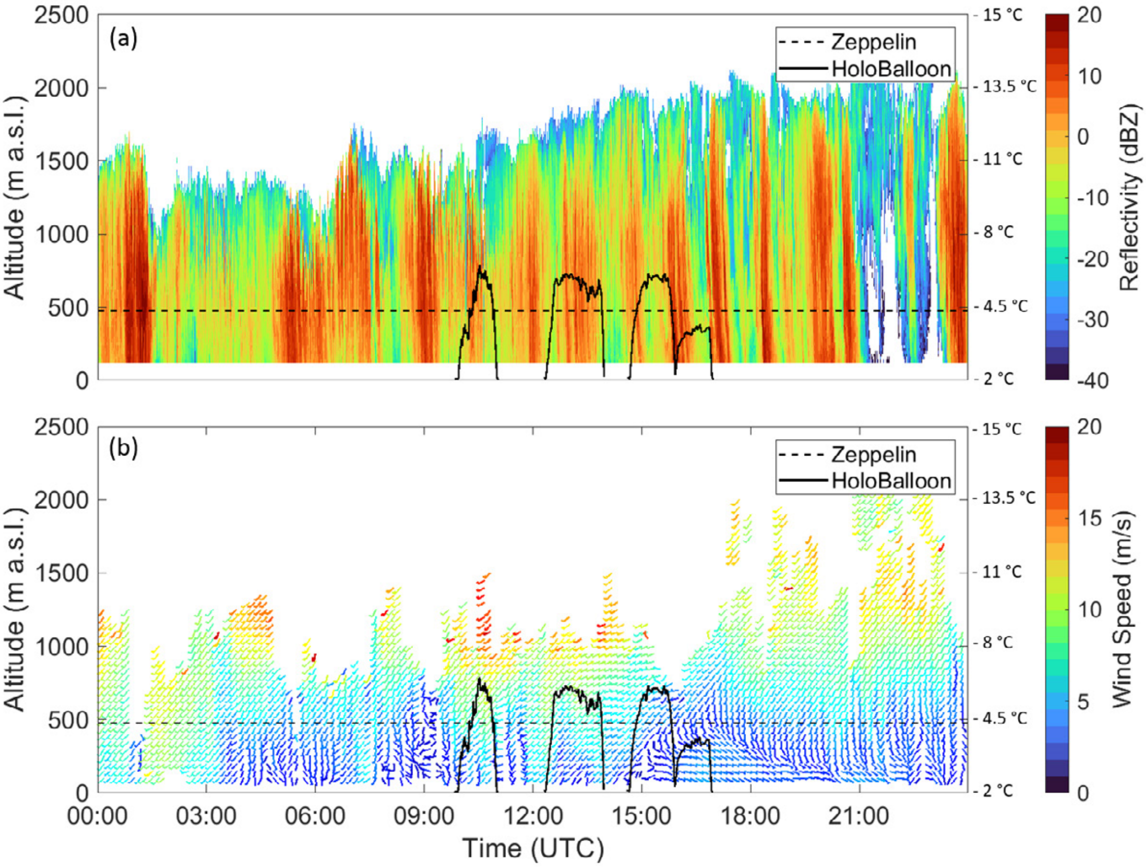

FIG. S2. Cloud radar and wind lidar measurements on 12 November 2019. (a) Cloud radar reflectivity and (b) wind lidar horizontal wind speed. The wind barbs show the wind direction and the color the horizontal wind speed. The solid black line shows the height of HoloBalloon and the dashed line the height of the Zeppelin Observatory. The black dots in (a) show the cloud base heights measured by the ceilometer. The temperature measured by the radiosonde launch at 1700 UTC is shown on the right y-axis at the corresponding altitude on the left y-axis.

Accepted for publication in *Bulletin of the American Meteorological Society*. DOI 10.1175/BAMS-D-21-0034.1.

On 12 November 2019, several short and intense precipitation events occurred and are recognizable as fallstreaks in the radar reflectivity (Fig. S2a) with total precipitation summing up to about 2.4 mm (not shown). The large-scale wind measured by the radiosondes (Fig. S7) and visible on the wind lidar measurements above 800 m a.s.l. (Fig. S2b) was southwesterly. After 1500 UTC, a strong change in the horizontal wind direction below 500 m a.s.l. was observed, which generated strong wind shear (Fig. S2b). The Zeppelin Observatory was in cloud for large parts of the day and three flights into clouds were performed with HoloBalloon (Fig. S2).

S2. Swiss Site

S1. Aerosol measurements at the container

During October - November 2019 and March - April 2020, the temporary Swiss Site was installed at the southwestern end of Ny-Ålesund. Ambient aerosol, cloud condensation nuclei (CCN), and ice nucleating particles (INPs) were sampled through an inlet mounted on top of the observatory container. Aerosol particles were measured in the size range of 10 nm to 20 µm using an APS, scanning mobility particles sizer (SMPS, TSI Inc., Shoreview, MN, USA), condensation particle counters (CPC, TSI Inc., Shoreview, MN, USA), and optical particle counters (OPC-N3, Alphasense). A Wideband Integrated Bioaerosol Sensor (WIBS-NEO) provided information on fluorescent properties of the particles.

To obtain a broader INP concentration - temperature spectrum, two methods were applied in parallel. INPs were monitored continuously at -30 °C in the immersion freezing mode using the online technique Horizontal Ice Nucleating Chamber (HINC, Lacher et al. 2017). HINC sampled ambient air continuously at a total flow rate of 2.83 StdL min^{-1}, of which 90% consists of recirculating particle-free sheath flow and the remaining 10% is compensated by aerosol flow. To account for the false positive ice count originating from the internal chamber, e.g., falling frost from the warmer plate, a motorized valve was applied to switch from sample flow to filtered air measurements regularly (5 min) before and after each sampling period (15 min) to determine a background count. In addition, ambient aerosol particles were sampled from the heated inlet using a high flow-rate impinger (Coriolis® µ, Bertin Instruments, France) operating at 300 L min^{-1}. For one sample the impinger collected aerosol for one hour, probing a volume of 18 m^3. Right after collection, each sample was analysed for INP concentration via the offline technique DRoplet Ice Nuclei Counter Zurich (DRINCZ, David et al. 2019), which measured INP concentrations at sub-freezing temperatures down to -20°C. See also Wieder et al. (2022), where the setup and procedure are described in details.

CCN concentrations during the NASCENT campaign were measured by a cloud condensation nuclei counter (model CCNC-100), commercialized by Droplet Measurement Technologies (DMT, Longmont, CO, USA). Unfortunately, this instrument malfunctioned during periods of the campaign that include 12 November 2019. Therefore, we used a back-integrated SMPS to calculate the aerosol concentration down to a particle mobility diameter of 70 nm to estimate CCN concentrations, following the method by Koike et al. (2019). Data quality was ensured by comparing total integrated concentration with two condensation particle counters (CPC, TSI Inc., Shoreview, MN, USA) at the Zeppelin Observatory and an SMPS and a CPC at sea level at the Swiss Site.

Additionally, at regions near shore close to Ny-Ålesund, we used a clean glass plate withdrawn vertically from the sea surface for sea surface microlayer samples. The thin microlayer film on the plate was then transferred into sample bottles using a Teflon scraper to wipe down the glass plate. The sub-surface bulk seawater samples were sampled by directly submerging sample bottles to about 50 cm below the ocean surface.

S2. HoloBalloon

The tethered balloon system HoloBalloon (Ramelli et al. 2020) was used to perform in-situ cloud microphysical measurements. The main instrument on HoloBalloon is the HOLographic cloud Imager for Microscopic Objects (HOLIMO3B), which can image an ensemble of cloud particles in the size range from small cloud droplets (6 µm) to precipitation-sized particles (2 mm) in a three-dimensional sample volume (Henneberger et al. 2013; Beck et al. 2017; Ramelli et al. 2020). HOLIMO3B provides information about the phase-resolved particle size distribution and particle habits. Particles larger than 25 µm can be differentiated between cloud droplets and ice crystals based on their shape, whereas all particles smaller than 25 µm are classified as cloud droplets. Because of this size threshold, the reported ice properties can be considered as a lower estimate. Cloud droplets and ice crystals larger than 25 µm were classified using convolutional neural network trained on cloud particles from holographic imagers (Touloupas et al. 2020) and smaller cloud droplets using support vector machines. The ice particle habits were classified manually. The sampling volume of HOLIMO3B used was about 15.5 cm^{-3}, and 6 frames were taken per seconds. The processed data are averaged over 60 seconds, which gives a volume of about 5.6 L per minute. The diameter used from the measurements by HOLIMO3B is the major diameter, which correspond to the major axis of an ellipse around the detected pixels of the particle. Two OPCs and one 3D-sonic anemometer are furthermore mounted on the platform. Expanding on the measurement platform described in Ramelli et al. (2020), two pyranometers and pyrgeometers (Apogee SL-510/610, SP-510/610) measured upward and downward solar and terrestrial radiation were installed on the instrument and the platform was suspended 12 m below the helikite to prevent turbulence effects.

S3. Zeppelin Observatory

Detailed in-situ observations of clouds, aerosols, and meteorology were made at the Zeppelin Observatory. Figure S3 presents a schematic of the set-up at the site during NASCENT which is described below.

S1. GCVI sampling and aerosol instrumentation

A ground-based counterflow virtual impactor inlet (CVI) was installed at the Zeppelin Observatory to sample ambient cloud droplets and ice crystals. The CVI is based on the technical principles described by Shingler et al. (2012). The evaluation of the ground-based version of the CVI at the Zeppelin Observatory is described in detail by Karlsson et al. (2021). The CVI separates particles according to their inertia using opposing air flows. Large particles (e.g. cloud droplets or ice crystals) are sampled, while small particles with low inertia (e.g. interstitial aerosol) do not penetrate through the virtual stagnation plate of the inlet and are not sampled. The cloud droplets or ice crystals are then dried and the remaining particles are termed cloud residuals. The residuals are then characterized by various aerosol instruments. This includes a custom-made DMPS (differential mobility particle sizer) for measuring the particle size distribution between approximately 10 and 945 nm (electrical mobility diameter) (Karlsson et al. 2021). A CPC (Model 3772, TSI Inc, USA) determines the total particle number concentration. A multi-parameter bioaerosol spectrometer (MBS, University of Hertfordshire, U.K., see e.g., Ruske et al. 2017) characterizes the size, shape and fluorescent characteristics of particles larger than 0.5 μm (optical diameter). The FIGAERO-CIMS (see next section) was connected to the CVI to measure the chemical composition of cloud residuals and aerosol particles. An impactor sampler (AS-24W, Arios Inc., Tokyo, Japan) was used to collect particles for a single particle analysis using a transmission electron microscope (TEM; JEM-1400, JEOL) with an energy-dispersive X-ray spectrometer (EDS; X-max

80, Oxford Instruments). The extended-range single-particle soot photometer (SP2-XR, DMT Inc., USA Stephens et al. 2003; Schwarz et al. 2006) was used to characterize the black carbon content of cloud residuals. In addition, a cloud condensation nuclei counter (CCNC, DMT Inc., USA, see Roberts and Nenes 2005) measured the (re-)activation of cloud residuals behind the CVI.

The CVI can be operated in manual or automatic mode. In automatic mode, the readings of a visibility sensor were used to turn on the CVI (threshold was usually set to 1 km visibility). A three-way valve enables the in-situ instrumentation to sample from the whole-air inlet during non-cloudy periods, allowing additional validation with the standard aerosol instruments measuring behind the whole-air inlet.

An iodide chemical ionization high-resolution time-of-flight mass spectrometer (FIGAERO, Lopez-Hilfiker et al. 2014; Thornton et al. 2020) was coupled to a filter inlet for gases and aerosols (CIMS) using iodide-adduct ionization. The iodide-FIGAERO-CIMS is sensitive to polarizable or acidic organic aerosol components (Lee et al. 2014). The instrument was connected with two separate inlet lines to ambient air. The particle phase inlet was connected via a ½ inch stainless steel tube to a three-way valve switching between the whole air inlet and the CVI inlet mounted at the top of the observatory. During the NASCENT campaign aerosol particles were sampled with 4 L min^{-1} on a Teflon filter for 2.5 hours. To determine the particle background, air was passed through an additional Teflon filter upstream the FIGAERO particle inlet, usually every third collection cycle. The data presented here is particle phase data of one whole-air inlet sample and one CVI inlet sample (cloud residual). The gas phase inlet was connected via ¼ inch PTFE tubing to ambient air directly through a hole in the wall. Gases were sampled at 1 Hz with 2 StdL min^{-1}. To determine the gas phase background during the campaign, zero air was frequently injected into the instrument for 15 minutes.

The black carbon (BC) mass concentration was determined using an extended-range single-particle soot photometer (SP2-XR, Stephens et al. 2003; Schwarz et al. 2006), a multi-angle absorption photometer (MAAP, Petzold and Schönlinner 2004), and a continuous soot monitoring system (COSMOS, Kondo et al. 2011). Note that the measurement of BC mass relies on operational definitions and is therefore method dependent, as discussed by Petzold et al. (2013). Recently, a method to harmonize Arctic BC measurements using the COSMOS as a standard instrument was developed, because COSMOS-derived BC mass concentration is traceable to a rigorously calibrated SP2 and the absolute accuracy has been demonstrated previously to be about 15 % in the Arctic (Ohata et al. 2021, submitted). The agreement between the BC mass concentration measurements obtained during NASCENT indicates that the instruments are in accordance with this method.

On the terrace of Zeppelin Observatory, a Fine dust measurement device Fidas 200 S (FIDAS, Palas GmbH, Germany) was installed to measure the particle size distribution from around 200 nm to approx. 18 µm (optical diameter). The instrument is installed in its own temperature-controlled stainless steel water protected cabinet and the inlet pipe is automatically heated to ensure sampling at dry conditions.

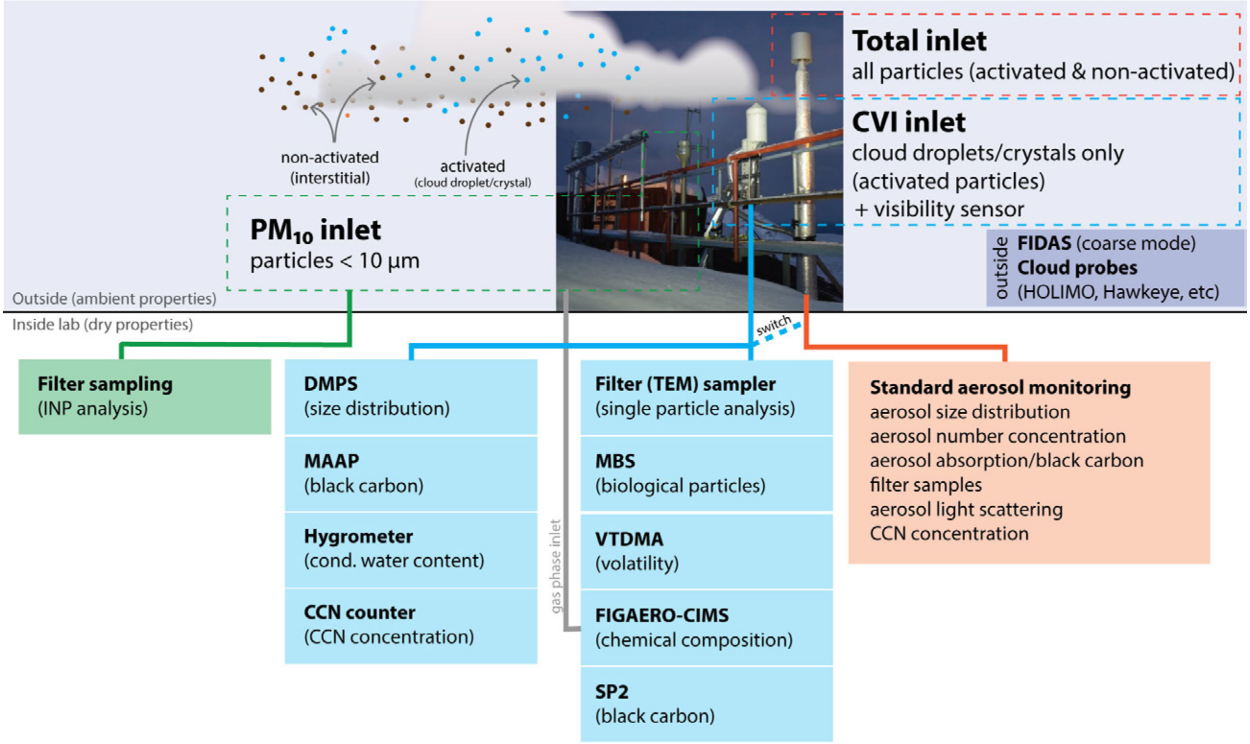

FIG. S3. Aerosol and cloud sampling at the Zeppelin Observatory during NASCENT. Various air inlet systems were used to sample particles, gas phase, cloud particles and whole air (aerosol and cloud particles) that were analysed in the laboratories below. In addition, various cloud probes and aerosol instrumentation were placed outside on the observation terrace. For further details on the CVI/whole-air inlet sampling see Karlsson et al. (2021).

Weekly aerosol sampling for measuring INPs active in the immersion mode at the Zeppelin Observatory has been performed continuously and sequentially from Sunday (0000 UTC) to Saturday (2359 UTC) using a 10-line Global Sampler (GS-10N, Tokyo Dylec Corp.) connected with a PM10 common inlet. Each sample has been collected on a precleaned Whatman Nuclepore track-etched membrane filter (47 mm in diameter and 0.2 µm in pore size) supported by a filter cassette screen (part no 59-005147-0010, Thermo Fisher Scientific) and mounted in a NILU inline filter holder system at a flow rate of 3 L min^{-1}. The samples were analyzed using the Cryogenic Refrigerator Applied to Freezing Test (CRAFT, Tobo 2016). The basic procedures for measuring

Accepted for publication in *Bulletin of the American Meteorological Society*. DOI 10.1175/BAMS-D-21-0034.1.

the number concentrations of atmospheric INPs using the CRAFT system are essentially the same as those used for our previous studies (Tobo et al. 2019, 2020). During the NASCENT campaign, we quantified the INP number concentrations over a temperature range down to -30°C.

Continuous year-round in-situ measurements of cloud and precipitating particles were made using a fog monitor (FM-120, DMT Inc., CO USA), Meteorological Particle Sensor (MPS, DMT Inc., CO USA), and Hawkeye (SPEC Inc., CO USA), which were located on the deck of the Zeppelin Observatory (Koike et al. 2019, 2021). The MPS is an optical disdrometer, which measures the precipitating particle size distributions with radii between 12.5 and 775 µm (12.5 µm resolution) using an optical array detector. In this study a maximum width is used as the particle size.

Hawkeye consists of three systems, namely, the Fast Cloud Droplet Probe (FCDP), the Two-Dimensional Stereo Particle Imaging Probe (2D-S), and the Cloud Particle Imager (CPI). The 2D-S has two optical array detectors which are orthogonal to each other and normal to the flow of particles. Each detector measures particles with radii between 10 and 1280 µm (10 µm resolution) and 50 and 6400 µm (50 µm resolution). The CPI is a particle imaging system using the CCD camera with an effective pixel size of 2.3 µm. In this study, a maximum dimension is used as the particle size. The 2D-S and CPI measure particles, which are sucked into a straight flow tube of the Hawkeye probe using an aspiration fan. The probe is mounted on a rotating pedestal to orient it toward the wind direction.

On 12 November 2019, the 2D-S observed ice crystals consisting of column and frozen drops that we named ’droplet lollipops’ in the main manuscript (Fig. S4). Such droplet lollipops were also measured by HOLIMO3B on HoloBalloon (see Fig. 10 of the main manuscript) and by HOLIMO3G at the Zeppelin Observatory (not shown).

Fig. S4. Example of ice crystals classified to 'droplet lollipops' observed with the 2D-S probe at the Zeppelin Observatory.

The holographic imager HOLIMO3G (Henneberger et al. 2013; Beck et al. 2017; Lauber et al. 2021) was installed at the Zeppelin Observatory. The working principle of HOLIMO3G is identical with the one of HOLIMO3B (see Section S2). The sampling volume of HOLIMO3G used in this study was about 13 cm^{-3}, and 1 frame was taken per second. The processed data are averaged over 30 seconds, which gives a volume of about 0.4 L per 30 sec interval.

S4. AWIPEV

The German Alfred Wegener Institute for Polar and Marine Research (AWI) and the French Polar Institute Paul Emile Victor (IPEV) operate their research stations in the town of Ny-Ålesund as the joint AWIPEV Research Base. Meteorological surface measurements are sampled continuously on the measurement field south of the Ny-Ålesund village, including up- and downward short- and longwave surface radiation measurements that are performed within the Baseline Surface

Radiation Network (BSRN, Maturilli et al. 2013, 2015). Radiosondes are launched at least once per day (Maturilli and Kayser 2017), with additional launches performed during intensive measurement periods. Cloud particle observations using a cloud particle sensor sonde (CPS sonde, Meisei Electric Co., Ltd.) were conducted at the AWIPEV in March 2019. The CPS sondes connected to the Meisei RS-11G radiosondes measure the vertical profile of cloud parameters (e.g., total particle count, particle phases, and particle size) and basic meteorological parameters (e.g., temperature, relative humidity, wind speed) (Inoue et al. 2021). Additionally, a suite of remote sensing instruments observe the atmosphere. In this study, we used the 94 GHz cloud radar of University of Cologne (JOYRAD-94, Küchler et al. 2017), the ceilometer (Vaisaila-CL51, Maturilli and Ebell 2018), and the wind lidar (Windcube200). The measurements of the cloud radar, the microwave radiometer HATPRO and the ceilometer are combined with thermodynamic profiles from a numerical weather prediction model to provide continuous, standardized information on cloud properties using the Cloudnet algorithm suite (Illingworth et al. 2007). For details on the Ny-Ålesund set-up, see Nomokonova et al. (2019). Further examples of the use of the Cloudnet products in Ny-Ålesund are given in Nomokonova et al. (2020) and Gierens et al. (2020). In this work, we utilized the vertically resolved hydrometeor classification to derive the monthly frequency of occurrence for different cloud types during the NASCENT year (Section 3b, Fig. 2b).

S1. Forward simulation with PAMTRA

To illustrate how different hydrometeors contribute to the radar Doppler spectrum (Section 4b, Fig. 11), we utilized the Passive and Active Microwave radiative TRAnsfer tool (PAMTRA Mech et al. 2020). PAMTRA produces synthetic observations for a given atmospheric state by combining a radiative transfer model with an instrument model. In the simulations carried out for this paper, PAMTRA was run in full Doppler spectra mode for a ground based view to produce synthetic cloud radar observations resembling the JOYRAD-94 measurements. In short, PAMTRA first calculates the volumetric backscattering as a function of particle size η_D, where D is the maximum diameter of the particle, based on the given hydrometeor properties and chosen scattering model. In the next step, η_D is converted to a spectral radar reflectivity as a function of particle fall velocity (e.g. the radar Doppler spectrum) by utilizing a hydrodynamic model, which provides a relationship between particle size and fall velocity. To produce radar Doppler spectra that are comparable to real observations, the radar simulator also accounts for kinematic broadening, vertical wind speed, radar receiver noise, and attenuation (Mech et al. 2020, and references therein).

In this work, the simulated radar observations were considered at a fixed altitude of 350 m, with 4 m range resolution. Further radar simulator settings corresponded to the parameters of the JOYRAD-94 measurements. The thermodynamic profile was obtained from the sounding launched at 1400 UTC. The vertical wind was set to 0 $\mathrm{ms^{-1}}$, and the eddy dissipation rate to 10^{-4} $\mathrm{m^2s^{-3}}$. Keeping these parameters constant is not realistic, but simplifies the interpretation of the simulated Doppler spectra as all changes can be attributed to changes in the hydrometeor properties, and changing thermodynamic conditions or range dependent factors of the radar measurement can be ignored. Additionally, attenuation was neglected for simplicity.

To produce the Doppler spectra shown in Fig. 11, a simulation was run for each hydromeoteor class independently. Two simulations were run for liquid hydrometeors: one for cloud droplets (≤56 µm) and one for drizzle droplets (>56 µm). Finally, a simulation including all hydrometeor classes was performed, and the resulting reflectivity showed reasonable agreement with the reflectivity measured by JOYRAD-94 (not shown).

S5. Gruvebadet

At Gruvebadet the long-term aerosol monitoring set of measurements including an SMPS + APS system (measuring the ambient aerosol size distribution) and filter-samplers deployed for the offline chemical characterization of PM10 as described in Udisti et al. (2016); Giardi et al. (2016); Becagli et al. (2019); Turetta et al. (2021) was operational. During NASCENT, ambient PM1 was collected on pre-baked quartz-fiber filters for the characterization of the Organic Matter and Organic Nitrogen using advanced spectroscopic techniques (proton-Nuclear Magnetic Resonance spectroscopy (H-NMR, Decesari et al. 2000) and C and N elemental analysis (CN-EA, Rinaldi et al. 2007; Montero-Martínez et al. 2014)). Due to the necessity of collecting sufficient amounts of samples for the subsequent detailed chemical analyses, long (~3-4 days) time-integrated samplings were performed. Multivariate statistical techniques will be applied on OM HR-TOF-AMS and NMR with the aim of the apportionment of different OA primary and secondary sources and components (Paglione et al. 2014).

In this study, a Particle Soot Absorption Photometer (PSAP - Radiance Research) which measures light absorption coefficient at three wavelengths is used. Measurements are corrected according to Virkkula et al. (2005) and normalized at standard temperature and pressure. Equivalent BC (eBC) concentration is derived from light absorption coefficient at 660 nm.

FIG. S5. Data availability (in percent) for the main instrumentation used at the different measurement sites during the NASCENT year.

S6. Climate Change Tower

The 33 m high Amundsen-Nobile Climate Change Tower (CCT) is equipped with a consistent set of meteorological sensors installed at 10 m and 33 m and described in Mazzola et al. (2016). Additionally, a wind lidar gives information about the vertical wind profile.

S7. WRF Modeling

The model used is the Advanced Research WRF model (ARW), version 4.2.1 Skamarock et al. (2019). We used a nested setup with three domains, where the outermost has a resolution of 15 km, the middle domain has 5 km and the inner has 1 km resolution. The geographical extent of the domains is shown in Figure S6.

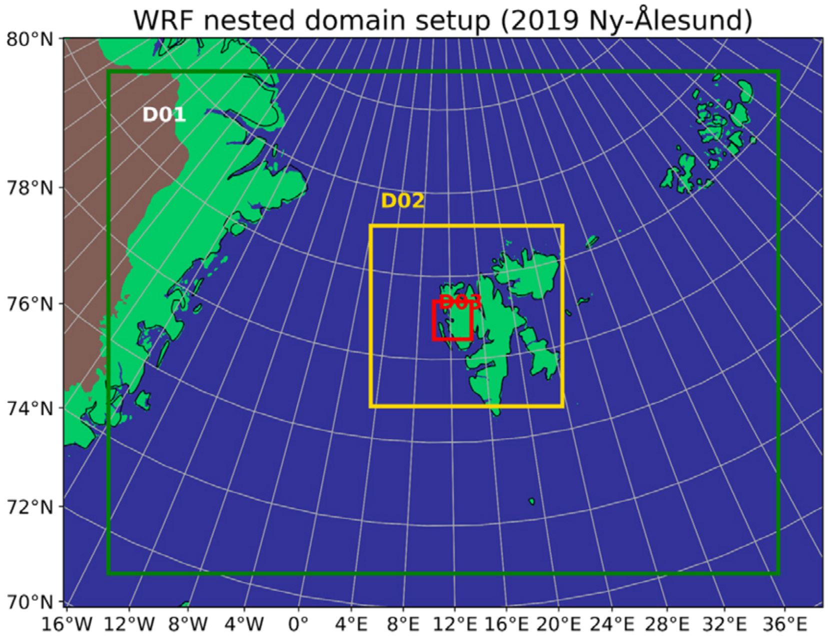

FIG. S6. Visualisation of the WRF domains with the outermost domain in green, in yellow the middle domain, and in red the inner domain.

The number of vertical levels is 172 between the surface and 50 hPa whereof 93 are below 3 km altitude. We initialized and nudged the model with 6-hourly reanalysis input data from ERA5 on single and pressure levels (Hersbach et al. 2018a,b). The longwave and shortwave radiation were treated by the CAM scheme (Collins et al. 2004), and for boundary layer processes we used the Yonsei University (YSU) scheme (Hong et al. 2006). As a microphysics scheme we used the double moment scheme developed by Milbrandt and Yau having six different classes for cloud water and ice, rain, snow, graupel and hail (Milbrandt and Yau 2005). Cumulus parametrization was only active on the largest domain, here we used the Grell-Freitas ensemble scheme (Grell and Freitas 2014). We verified a satisfying model performance by comparing meteorological results with radiosonde observations before using the model data for comparison of cloud properties (Fig. S7). The CCN and INP concentrations were prescribed and are therefore independent of the simulated background aerosol.

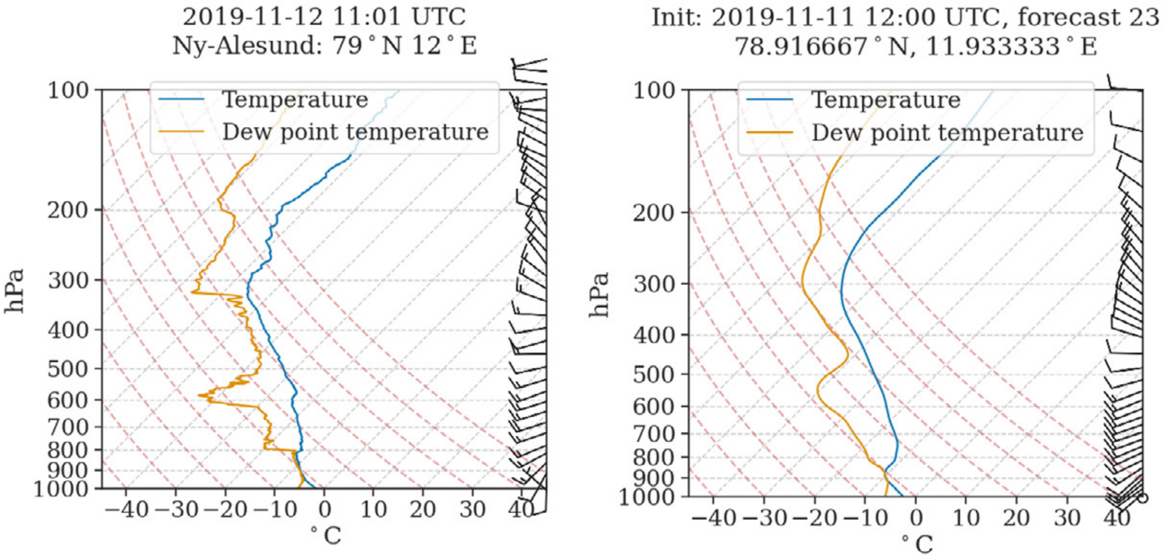

FIG. S7. Radiosounding at 1100 UTC 12 November 2019 performed at Ny-Ålesund (left) and simulated with the WRF model (right).

To complement the description of the WRF simulation for flight 3 in Section 4.c of the main manuscript, we show here the simulated cloud properties averaged for each flights performed with HoloBalloon on 12 November 2019 (Fig. S8). The model correctly simulated an increase in the cloud top height from flight 1 to 3 as can be seen from the increasing height where hydrometeors are observed (Fig. S9). This is in accordance with the cloud top increase measured by the cloud radar (Fig. S3,S9). It also followed observed changes in cloud base height in agreement with ceilometer retrievals, although the magnitude of the decrease before the third flight differs (Fig. S8). In this regard, it is important to note that snowfall may have attenuated the visibility of the ceilometer below cloud base and thus led to a lower recorded liquid water cloud base than in reality.

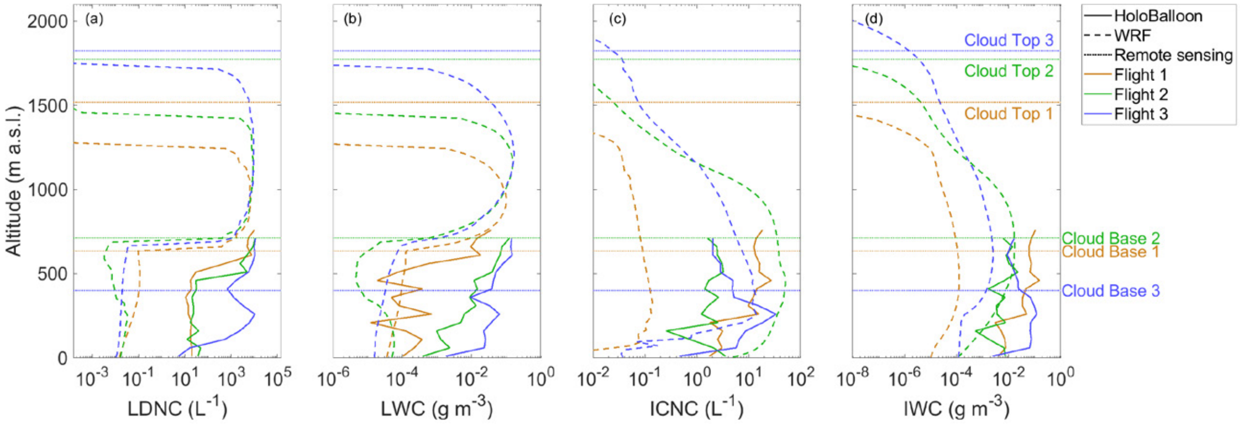

FIG. S8. The averaged vertical profiles during the three flights on 12 November 2019 (flight 1 from 1000 to 1100 UTC (yellow), flight 2 from 1215 to 1400 UTC (green), and flight 3 from 1545 to 1700 UTC (blue)) as observed by HOLIMO3B (solid lines) and simulated by WRF (dashed lines) of (a) CDNC, (b) LWC, (c) ICNC & (d) IWC. The data from HOLIMO3B are averaged over 50 m altitude bins and the WRF data over every model layer. The average cloud base and cloud top measured by the remote sensing instrumentation (ceilometer and cloud radar, respectively) are represented by the dotted horizontal lines. All frozen hydrometeor types (graupel, hail, snow and ice) from the WRF model are merged together into the ICNC and IWC calculation and the rain and cloud droplet number and mass for the CDNC and LWC calculation.

The liquid droplet number concentration (LDNC) and LWC measured by HOLIMO3B and simulated by the model are comparable between 600-750 m a.s.l (which corresponds approximately to cloud base for flights 1 and 2), whereas below this height the model underestimates the LDNC and LWC (Fig. S8a,b). The simulated ICNC and IWC are underestimated during flight 1, whereas during flight 2 the simulated ICNC is overestimated and the simulated IWC is in the same order of magnitude as the in-situ measurements (Fig. S8c,d).

References

Becagli, S., and Coauthors, 2019: Biogenic aerosol in the arctic from eight years of msa data from ny Ålesund (svalbard islands) and thule (greenland). *Atmosphere*, **10 (7)**, doi:10.3390/atmos10070349, URL https://www.mdpi.com/2073-4433/10/7/349.

Beck, A., J. Henneberger, S. Schöpfer, J. Fugal, and U. Lohmann, 2017: Hologondel: in situ cloud observations on a cable car in the Swiss Alps using a holographic imager. *Atmospheric Measurement Techniques*, **10 (2)**, 459–476, doi:10.5194/amt-10-459-2017.

Collins, W. D., and Coauthors, 2004: Description of the ncar community atmosphere model (cam 3.0). *NCAR Tech. Note NCAR/TN-464+ STR*, **226**.

David, R. O., and Coauthors, 2019: Development of the droplet ice nuclei counter zurich (drincz): validation and application to field-collected snow samples. *Atmospheric Measurement Techniques*, **12 (12)**, 6865–6888, doi:10.5194/amt-12-6865-2019.

Decesari, S., M. C. Facchini, S. Fuzzi, and E. Tagliavini, 2000: Characterization of water-soluble organic compounds in atmospheric aerosol: A new approach. *Journal of Geophysical Research: Atmospheres*, **105 (D1)**, 1481–1489, doi:https://doi.org/10.1029/1999JD900950, URL https://agupubs.onlinelibrary.wiley.com/doi/abs/10.1029/1999JD900950, https://agupubs.onlinelibrary.wiley.com/doi/pdf/10.1029/1999JD900950.

Giardi, F., and Coauthors, 2016: Size distribution and ion composition of aerosol collected at ny-ålesund in the spring–summer field campaign 2013. *Rendiconti Lincei*, **27 (1)**, 47–58, doi:10.1007/s12210-016-0529-3, URL https://doi.org/10.1007/s12210-016-0529-3.

Gierens, R., S. Kneifel, M. D. Shupe, K. Ebell, M. Maturilli, and U. Löhnert, 2020: Low-level mixed-phase clouds in a complex arctic environment. *Atmospheric Chemistry and Physics*, **20 (6)**, 3459–3481, doi:10.5194/acp-20-3459-2020.

Grell, G. A., and S. R. Freitas, 2014: A scale and aerosol aware stochastic convective parameterization for weather and air quality modeling. *Atmospheric Chemistry and Physics*, **14 (10)**, 5233–5250.

Hellmuth, F., and S. Hofer, 2019: Weathermaps from meps latest runs. University of Oslo, Oslo, Norway, URL https://github.com/franzihe/Weathermap.

Henneberger, J., J. P. Fugal, O. Stetzer, and U. Lohmann, 2013: HOLIMO II: a digital holographic instrument for ground-based in situ observations of microphysical properties of mixed-phase clouds. *Atmospheric Measurement Techniques*, **6 (11)**, 2975–2987, doi: 10.5194/amt-6-2975-2013.

Hersbach, H., and Coauthors, 2018a: ERA5 hourly data on pressure levels from 1979 to present. *Copernicus Climate Change Service (C3S) Climate Data Store (CDS) (Accessed on 19-MAR-2021)*, doi:10.24381/cds.bd0915c6.

Hersbach, H., and Coauthors, 2018b: ERA5 hourly data on single levels from 1979 to present. *Copernicus Climate Change Service (C3S) Climate Data Store (CDS). (Accessed on 21-APR-2021)*, doi:10.24381/cds.adbb2d47.

Hong, S.-Y., Y. Noh, and J. Dudhia, 2006: A new vertical diffusion package with an explicit treatment of entrainment processes. *Monthly weather review*, **134 (9)**, 2318–2341.

Accepted for publication in *Bulletin of the American Meteorological Society*. DOI 10.1175/BAMS-D-21-0034.1.

Illingworth, A. J., and Coauthors, 2007: Cloudnet: Continuous evaluation of cloud profiles in seven operational models using ground-based observations. *Bulletin of the American Meteorological Society*, **88 (6)**, 883 – 898, doi:10.1175/BAMS-88-6-883.

Inoue, J., Y. Tobo, K. Sato, F. Taketani, and M. Maturilli, 2021: Application of cloud particle sensor sondes for estimating the number concentration of cloud water droplets and liquid water content: case studies in the arctic region. *Atmospheric Measurement Techniques*, **14 (7)**, 4971–4987, doi:10.5194/amt-14-4971-2021, URL https://amt.copernicus.org/articles/14/4971/2021/.

Karlsson, L., R. Krejci, M. Koike, K. Ebell, and P. Zieger, 2021: A long-term study of cloud residuals from low-level arctic clouds. *Atmospheric Chemistry and Physics*, **21 (11)**, 8933–8959, doi:10.5194/acp-21-8933-2021, URL https://acp.copernicus.org/articles/21/8933/2021/.

Koike, M., and Coauthors, 2019: Year-round in situ measurements of arctic low-level clouds: Microphysical properties and their relationships with aerosols. *Journal of Geophysical Research: Atmospheres*, **124 (3)**, 1798–1822, doi:10.1029/2018JD029802.

Koike, M., and Coauthors, 2021: Studies on arctic aerosols and clouds during the arcs project. *Polar Science*, **27**, 100 621, doi:https://doi.org/10.1016/j.polar.2020.100621, URL https://www.sciencedirect.com/science/article/pii/S1873965220301444, arctic Challenge for Sustainability Project (ArCS).

Kondo, Y., L. Sahu, N. Moteki, F. Khan, N. Takegawa, X. Liu, M. Koike, and T. Miyakawa, 2011: Consistency and traceability of black carbon measurements made by laser-induced incandescence, thermal-optical transmittance, and filter-based photo-absorption techniques. *Aerosol Science and Technology*, **45 (2)**, 295–312, doi:10.1080/02786826.2010.533215.

Küchler, N., S. Kneifel, U. Löhnert, P. Kollias, H. Czekala, and T. Rose, 2017: A W-Band Radar-Radiometer System for Accurate and Continuous Monitoring of Clouds and Precipitation. *J. Atmos. Oceanic Technol.*, **34**, 2375–2392, doi:10.1175/JTECH-D-17-0019.1.

Lacher, L., U. Lohmann, Y. Boose, A. Zipori, E. Herrmann, N. Bukowiecki, M. Steinbacher, and Z. A. Kanji, 2017: The horizontal ice nucleation chamber (hinc): Inp measurements at conditions relevant for mixed-phase clouds at the high altitude research station jungfraujoch. *Atmospheric Chemistry and Physics*, **17 (24)**, 15 199–15 224, doi:10.5194/acp-17-15199-2017.

Lauber, A., J. Henneberger, C. Mignani, F. Ramelli, J. T. Pasquier, J. Wieder, M. Hervo, and U. Lohmann, 2021: Continuous secondary-ice production initiated by updrafts through the melting layer in mountainous regions. *Atmospheric Chemistry and Physics*, **21 (5)**, 3855–3870, doi:10.5194/acp-21-3855-2021.

Lee, B. H., F. D. Lopez-Hilfiker, C. Mohr, T. Kurtén, D. R. Worsnop, and J. A. Thornton, 2014: An iodide-adduct high-resolution time-of-flight chemical-ionization mass spectrometer: Application to atmospheric inorganic and organic compounds. *Environmental Science & Technology*, **48 (11)**, 6309–6317, doi:10.1021/es500362a.

Lopez-Hilfiker, F. D., and Coauthors, 2014: A novel method for online analysis of gas and particle composition: description and evaluation of a filter inlet for gases and aerosols (figaero). *Atmospheric Measurement Techniques*, **7 (4)**, 983–1001, doi:10.5194/amt-7-983-2014.

Maturilli, M., and K. Ebell, 2018: Twenty-five years of cloud base height measurements by ceilometer in ny-ålesund, svalbard. *Earth System Science Data*, **10 (3)**, 1451–1456, doi:10.5194/essd-10-1451-2018.

Maturilli, M., A. Herber, and G. König-Langlo, 2013: Climatology and time series of surface meteorology in Ny-Ålesund, Svalbard. *Earth System Science Data*, **5 (1)**, 155–163, doi:10.5194/essd-5-155-2013.

Maturilli, M., A. Herber, and G. König-Langlo, 2015: Surface radiation climatology for Ny-Ålesund, Svalbard (78.9° N), basic observations for trend detection. *Theoretical and Applied Climatology*, **120 (1)**, 331–339, doi:10.1007/s00704-014-1173-4.

Maturilli, M., and K. Kayser, 2017: Arctic warming, moisture increase and circulation changes observed in the Ny-Ålesund homogenized radiosonde record. *Theoretical and Applied Climatology*, **130 (1-17)**, 1434–4483, doi:10.1007/s00704-016-1864-0.

Mazzola, M., A. P. Viola, C. Lanconelli, and V. Vitale, 2016: Atmospheric observations at the amundsen-nobile climate change tower in ny-Ålesund, svalbard. *Rendiconti Lincei*, **27 (27)**, 7–18, doi:10.1007/s12210-016-0540-8.

Mech, M., M. Maahn, S. Kneifel, D. Ori, E. Orlandi, P. Kollias, V. Schemann, and S. Crewell, 2020: Pamtra 1.0: the passive and active microwave radiative transfer tool for simulating radiometer and radar measurements of the cloudy atmosphere. *Geoscientific Model Development*, **13 (9)**, 4229–4251, doi:10.5194/gmd-13-4229-2020.

Milbrandt, J., and M. Yau, 2005: A multimoment bulk microphysics parameterization. Part II: A proposed three-moment closure and scheme description. *Journal of Atmospheric Sciences*, **62 (9)**, 3065–3081.

Montero-Martínez, G., M. Rinaldi, S. Gilardoni, L. Giulianelli, M. Paglione, S. Decesari, S. Fuzzi, and M. C. Facchini, 2014: On the water-soluble organic nitrogen concentration and mass size distribution during the fog season in the po valley, italy. *Science of The To-*

tal Environment, **485-486**, 103–109, doi:https://doi.org/10.1016/j.scitotenv.2014.03.060, URL https://www.sciencedirect.com/science/article/pii/S0048969714003908.

Nomokonova, T., K. Ebell, U. Löhnert, M. Maturilli, and C. Ritter, 2020: The influence of water vapor anomalies on clouds and their radiative effect at ny-ålesund. *Atmospheric Chemistry and Physics*, **20**, 5157–5173, doi:10.5194/acp-20-5157-2020.

Nomokonova, T., K. Ebell, U. Löhnert, M. Maturilli, C. Ritter, and E. O'Connor, 2019: Statistics on clouds and their relation to thermodynamic conditions at Ny-Ålesund using ground-based sensor synergy. *Atmospheric Chemistry and Physics*, **19 (6)**, 4105–4126, doi:10.5194/acp-19-4105-2019.

Ohata, S., and Coauthors, 2021: Estimates of mass absorption cross sections of black carbon for filter-based absorption photometers in the arctic. *Atmospheric Measurement Techniques*, **14 (10)**, 6723–6748, doi:10.5194/amt-14-6723-2021, URL https://amt.copernicus.org/articles/14/6723/2021/.

Paglione, M., and Coauthors, 2014: Primary and secondary biomass burning aerosols determined by proton nuclear magnetic resonance (^{1}h-nmr) spectroscopy during the 2008 eucaari campaign in the po valley (italy). *Atmospheric Chemistry and Physics*, **14 (10)**, 5089–5110, doi:10.5194/acp-14-5089-2014, URL https://acp.copernicus.org/articles/14/5089/2014/.

Petzold, A., and M. Schönlinner, 2004: Multi-angle absorption photometry–a new method for the measurement of aerosol light absorption and atmospheric black carbon. *J. Aerosol Sci.*, **35 (4)**, 421–441.

Petzold, A., and Coauthors, 2013: Recommendations for reporting "black carbon" measurements. *Atmospheric Chemistry and Physics*, **13 (16)**, 8365–8379, doi:10.5194/acp-13-8365-2013, URL

Accepted for publication in *Bulletin of the American Meteorological Society*. DOI 10.1175/BAMS-D-21-0034.1.

https://acp.copernicus.org/articles/13/8365/2013/.

Ramelli, F., A. Beck, J. Henneberger, and U. Lohmann, 2020: Using a holographic imager on a tethered balloon system for microphysical observations of boundary layer clouds. *Atmospheric Measurement Techniques*, **13 (2)**, 925–939, doi:10.5194/amt-13-925-2020, URL https://amt.copernicus.org/articles/13/925/2020/.

Rinaldi, M., L. Emblico, S. Decesari, S. Fuzzi, M. C. Facchini, and V. Librando, 2007: Chemical characterization and source apportionment of size-segregated aerosol collected at an urban site in sicily. *Water, Air, and Soil Pollution*, **185 (1)**, 311–321, doi:10.1007/s11270-007-9455-4, URL https://doi.org/10.1007/s11270-007-9455-4.

Roberts, G. C., and A. Nenes, 2005: A continuous-flow streamwise thermal-gradient ccn chamber for atmospheric measurements. *Aerosol Science and Technology*, **39 (3)**, 206–221, doi:10.1080/027868290913988.

Ruske, S., D. O. Topping, V. E. Foot, P. H. Kaye, W. R. Stanley, I. Crawford, A. P. Morse, and M. W. Gallagher, 2017: Evaluation of machine learning algorithms for classification of primary biological aerosol using a new uv-lif spectrometer. *Atmos. Meas. Tech.*, **10 (2)**, 695–708, doi:10.5194/amt-10-695-2017, URL https://www.atmos-meas-tech.net/10/695/2017/.

Schwarz, J. P., and Coauthors, 2006: Single-particle measurements of midlatitude black carbon and light-scattering aerosols from the boundary layer to the lower stratosphere. *Journal of Geophysical Research: Atmospheres*, **111 (D16)**, doi:10.1029/2006JD007076, URL https://agupubs.onlinelibrary.wiley.com/doi/10.1029/2006JD007076.

Shingler, T., and Coauthors, 2012: Characterisation and airborne deployment of a new counterflow virtual impactor inlet. *Atmos. Meas. Tech.*, **5 (6)**, 1259–1269, doi:10.5194/amt-5-1259-2012, URL http://www.atmos-meas-tech.net/5/1259/2012/.

Skamarock, W. C., and Coauthors, 2019: A description of the advanced research wrf model version 4. *National Center for Atmospheric Research: Boulder, CO, USA*, 145.

Stephens, M., N. Turner, and J. Sandberg, 2003: Particle identification by laser-induced incandescence in a solid-state laser cavity. *Applied Optics*, **42 (19)**, 3726, doi:10.1364/AO.42.003726, URL https://www.osapublishing.org/abstract.cfm?URI=ao-42-19-3726.

Thornton, J. A., C. Mohr, S. Schobesberger, E. L. D'Ambro, B. H. Lee, and F. D. Lopez-Hilfiker, 2020: Evaluating organic aerosol sources and evolution with a combined molecular composition and volatility framework using the filter inlet for gases and aerosols (figaero). *Accounts of Chemical Research*, **53 (8)**, 1415–1426, doi:10.1021/acs.accounts.0c00259.

Tobo, Y., 2016: An improved approach for measuring immersion freezing in large droplets over a wide temperature range. *Scientific Reports*, **6 (1)**, 32 930, doi:10.1038/srep32930.

Tobo, Y., J. Uetake, H. Matsui, N. Moteki, Y. Uji, Y. Iwamoto, K. Miura, and R. Misumi, 2020: Seasonal trends of atmospheric ice nucleating particles over tokyo. *Journal of Geophysical Research: Atmospheres*, **125 (23)**, e2020JD033 658, doi:https://doi.org/10.1029/2020JD033658, e2020JD033658 2020JD033658-T.

Tobo, Y., and Coauthors, 2019: Glacially sourced dust as a potentially significant source of ice nucleating particles. *Nature Geoscience*, **12 (4)**, 253–258, doi:10.1038/s41561-019-0314-x.

Touloupas, G., A. Lauber, J. Henneberger, A. Beck, and A. Lucchi, 2020: A convolutional neural network for classifying cloud particles recorded by imaging probes. *Atmospheric Measurement Techniques*, **13 (5)**, 2219–2239, doi:10.5194/amt-13-2219-2020, URL https://amt.copernicus.org/articles/13/2219/2020/.

Turetta, C., M. Feltracco, E. Barbaro, A. Spolaor, C. Barbante, and A. Gambaro, 2021: A year-round measurement of water-soluble trace and rare earth elements in arctic aerosol: Possible inorganic tracers of specific events. *Atmosphere*, **12 (6)**, doi:10.3390/atmos12060694, URL https://www.mdpi.com/2073-4433/12/6/694.

Udisti, R., and Coauthors, 2016: Sulfate source apportionment in the ny-ålesund (svalbard islands) arctic aerosol. *Rendiconti Lincei*, **27 (1)**, 85–94, doi:10.1007/s12210-016-0517-7, URL https://doi.org/10.1007/s12210-016-0517-7.

Virkkula, A., N. C. Ahlquist, D. S. Covert, W. P. Arnott, P. J. Sheridan, P. K. Quinn, and D. J. Coffman, 2005: Modification, calibration and a field test of an instrument for measuring light absorption by particles. *Aerosol Science and Technology*, **39 (1)**, 68–83, doi:10.1080/027868290901963, URL https://doi.org/10.1080/027868290901963, https://doi.org/10.1080/027868290901963.

Wieder, J., and Coauthors, 2022: Unveiling atmospheric transport and mixing mechanisms of ice-nucleating particles over the alps. *Atmospheric Chemistry and Physics*, **22 (5)**, 3111–3130, doi:10.5194/acp-22-3111-2022, URL https://acp.copernicus.org/articles/22/3111/2022/.

Accepted for publication in *Bulletin of the American Meteorological Society*. DOI 10.1175/BAMS-D-21-0034.1.

TABLE 1. Overview of all instruments and derived parameters installed in the framework of NASCENT or used in this study. Note that more instrumentation is operational at Ny-Ålesund.

Location	*Instrument*	*Derived Parameters*
Zeppelin Observatory	Ultrasonic Anemometer	Wind speed and direction
	Ground-based virtual impactor inlet (GCVI)	Operational parameters (flows, temperature, visibility, etc)
	Multiparameter Bioaerosol Sensor (MBS)	Optical parameters on particle size, shape and fluorescence (single-particle data)
	Chemical ionization mass spectrometer with filter inlet for gases and aerosols (FIGAERO-CIMS)	Mass spectra: ion signals in counts per second
	Differential Mobility Particle Sizer (DMPS 1&2)	Particle size distribution (5 to 900 nm) and particle concentration
	HOLIMO3G	Phase resolved distribution, ICNC, CDNC, IWC, LWC
	Hawkeye	Particle size distributions (3 - 50 µm)
	MPS	Precipitating particle size distributions (12.5 - 775 µm)
	CDP2	cloud droplet number concentration (2 µm - 50 µm)
	CRAFT	INP number concentration (immersion mode)
	Extended range Single Particle Soot Photometer (SP2-XR)	Black carbon mass concentrations and size distributions for normal ambient aerosol as well as for cloud droplet residuals (sampled from the CVI inlet)
	SP2-XR	Black carbon mass concentrations and size distributions for normal ambient aerosol as well as for cloud droplet residuals (sampled from the CVI inlet)
	MAAP	Equivalent black carbon mass concentrations
	COSMOS	Equivalent black carbon mass concentrations
	CPC, DMPS, SMPS	Ambient aerosol size distribution
	Fog monitor	cloud droplet size distribution

Accepted for publication in *Bulletin of the American Meteorological Society*. DOI 10.1175/BAMS-D-21-0034.1.

Swiss Site	APS, SMPS, CPC, OPC	Ambient aerosol size distribution
	Weather station	Meteorological variables
	Laserdisdrometer	Precipitation rate, particle size and fall velocity distribution
	DRINCZ	INP concentration in ambient air, snow, rime and snow pits
	HINC	Continuous ambient INP concentration measurement (< 2.5,µm , T = 243.15 K, RHw = 104%)
	WIBS-NEO	Size distribution and fluorescence of aerosol particles
	CCN-100 Counter	Count and size of CCN
HoloBalloon	HOLIMO3B	Phase resolved distribution, ICNC, CDNC, IWC, LWC
	Sonic Anemometer	Wind speed and direction
	OPC	Ambient aerosol size distribution
	Pyranometer & Pyrgeometer	SW & LW up & down
AWIPEV	94 GHz Doppler Cloud Radar JOYRAD-94 (RPG-FMCW-94-SP)	Radar reflectivity factor, radar Doppler spectra and its moments
	Wind Lidar Windcube200	Wind direction and speed profile
	Laserdisdrometer OTT Parsivel^2	Precipitation rate, particle size and fall velocity distribution
	Vaisala CL-51 ceilometer	Attenuated backscatter, cloud base height
	Digiquarz-6000, PT100, Vaisala HMT337, Thiess combined wind sensor classic	Station level pressure, temperature (2 and 10 m), relative humidity (2 m), wind speed and direction (2 and 10 m)
	Radiosondes RS41	Profiles of T, p, RH, wind vector
	CPS sonde	Profiles of cloud parameters (e.g., total particle count, particle phases, and particle size) and of T, p, RH, wind vector
Gruvebadet	PM10 filter sampling with subsequent offline analysis via DRINCZ	Ambient INP concentration - temperature spectrum
	Particle Soot Absorption Photometer (PSAP)	equivalent Black Carbon concentration
	PM1 filter samples with subsequent offline with H-NMR and HR-TOF-AMS	Organic Matter characterization
	PM1 and PM10 with subsequent offline analysis via DFPC	INP concentraion (condensation freezing)
CCT	Sonic Young Anemometer	Wind speed and direction